

# Mysteriously high $\Delta^{14}\text{C}$ of the glacial atmosphere: Influence of $^{14}\text{C}$ production and carbon cycle changes

Ashley Dinauer<sup>1,\*</sup>, Florian Adolphi<sup>1,2</sup>, Fortunat Joos<sup>1</sup>

<sup>1</sup>Climate and Environmental Physics, Physics Institute and Oeschger Centre for Climate Change Research, University of Bern, Sidlerstrasse 5, 3012 Bern, Switzerland

<sup>2</sup>Quaternary Sciences, Department of Geology, Lund University, Sölvegatan 12, 22362 Lund, Sweden

\*To whom correspondence should be addressed. Email: ashley.dinauer@climate.unibe.ch

**Abstract.** Despite intense focus on the  $\sim 190$  permil drop in atmospheric  $\Delta^{14}\text{C}$  during Heinrich Stadial 1  $\sim 17.4$  to 14.6 kyr BP, the specific mechanisms responsible for the apparent  $\Delta^{14}\text{C}$  excess in the glacial atmosphere have received considerably less attention. The computationally efficient Bern3D earth system model of intermediate complexity, designed for long-term climate simulations, allows us to address a very fundamental but still elusive question concerning the atmospheric  $\Delta^{14}\text{C}$  record: How can we explain the persistence of relatively high  $\Delta^{14}\text{C}$  values during the millennia after the Laschamp event? Large uncertainties in the pre-Holocene  $^{14}\text{C}$  production rate, as well as in the older portion of the  $\Delta^{14}\text{C}$  record, complicate our qualitative and quantitative interpretation of the glacial  $\Delta^{14}\text{C}$  elevation. Here we begin with sensitivity experiments that investigate the controls on atmospheric  $\Delta^{14}\text{C}$  in idealized settings. We show that the interaction with the ocean sediments may be much more important to the simulation of  $\Delta^{14}\text{C}$  than had been previously thought. In order to provide a bounded estimate of glacial  $\Delta^{14}\text{C}$  change, the Bern3D model was integrated with five available estimates of the  $^{14}\text{C}$  production rate as well as reconstructed and hypothetical paleoclimate forcing. Model results demonstrate that none of the available reconstructions of past changes in  $^{14}\text{C}$  production can reproduce the elevated  $\Delta^{14}\text{C}$  levels during the last glacial. In order to increase atmospheric  $\Delta^{14}\text{C}$  to glacial levels, a drastic reduction of air-sea exchange efficiency in the polar regions must be assumed, though discrepancies remain for the portion of the record younger than  $\sim 33$  kyr BP. We end with an illustration of how the  $^{14}\text{C}$  production rate would have had to evolve to be consistent with the  $\Delta^{14}\text{C}$  record, by combining an atmospheric radiocarbon budget with the Bern3D model. The overall conclusion is that the remaining discrepancies with respect to glacial  $\Delta^{14}\text{C}$  may be linked to an underestimation of  $^{14}\text{C}$  production and/or a biased-high reconstruction of  $\Delta^{14}\text{C}$  over the time period of interest. Alternatively, we appear to still be missing an important carbon cycle process for atmospheric  $\Delta^{14}\text{C}$ .

## 1 Introduction

The cosmogenic radionuclide radiocarbon ( $^{14}\text{C}$ ) is a powerful tracer for the study of several ocean processes including deep ocean circulation and ventilation. Past changes in atmospheric  $^{14}\text{C}/\text{C}$  (i.e.,  $\Delta^{14}\text{C}_{\text{atm}}$ , in permil; corresponding to  $\Delta$  from Stuiver and Polach, 1977), as recorded in absolutely dated tree rings, plant macrofossils, speleothems, corals,

37 and foraminifera, have been interpreted as possibly reflecting real changes in the ocean's large-scale overturning  
38 circulation (Siegenthaler et al., 1980). The extended 54,000-year record of  $\Delta^{14}\text{C}_{\text{atm}}$  from the latest IntCal compilation  
39 (i.e., IntCal13; Reimer et al., 2013) and from two Hulu Cave stalagmites (Cheng et al., 2018), adjusted to the presently  
40 accepted value of the radiocarbon half-life of 5700 years (Audi et al., 2003; Bé et al., 2013), suggests that large  
41 millennial-scale variations in  $\Delta^{14}\text{C}_{\text{atm}}$  have occurred during the last glacial, compared to the relatively small (~30 ppm)  
42 change in atmospheric  $\text{CO}_2$  over the same time period (Fig. 1). When interpreting the implications of such changes, it  
43 is important to note that  $\Delta^{14}\text{C}_{\text{atm}}$  is controlled not only by global carbon cycle processes but also by variations in the  
44 atmospheric  $^{14}\text{C}$  production rate. Therefore, the use of  $\Delta^{14}\text{C}_{\text{atm}}$  as an indicator of past oceanic conditions, particularly  
45 those associated with air-sea exchange efficiency and deep ocean ventilation rates, requires reliable estimates of the  
46  $^{14}\text{C}$  production rate over time.

47  
48 The vast majority of all  $^{14}\text{C}$  production changes are the result of either solar or geomagnetic modulation of  
49 the cosmic ray flux reaching the Earth (Masarik and Beer, 1999; Poluianov et al., 2016). Fig. 1 shows several different  
50 proxy records of the global production rate of  $^{14}\text{C}$  in relative units covering the full range of the  $^{14}\text{C}$  dating method,  
51 based on geomagnetic field data from marine sediments (Laj et al., 2000; Laj et al., 2004; Nowaczyk et al., 2013;  
52 Channell et al., 2018) and on  $^{10}\text{Be}$  and  $^{36}\text{Cl}$  measurements in polar ice cores (Adolphi et al., 2018). A fundamental  
53 difference between these reconstruction methods is that paleointensity-based estimates of the  $^{14}\text{C}$  production rate, by  
54 definition, do not reflect changes in the solar modulation of the cosmic radiation, whereas ice-core  $^{10}\text{Be}$ -based  
55 estimates give the combined influence of solar and geomagnetic modulation on radionuclide production. Of note is  
56 the striking coherence in all three records ( $\Delta^{14}\text{C}_{\text{atm}}$ , paleointensity-based production, and ice-core  $^{10}\text{Be}$ -based  
57 production) of the Laschamp excursion (~41 kyr BP), when the Earth's geomagnetic dipole field briefly reversed and  
58 its intensity was close to zero (Nowaczyk et al., 2012; Laj et al., 2014). According to reconstructions and production  
59 rate models, this large geomagnetic event caused a doubling of the  $^{14}\text{C}$  production rate, leading to the highest  $\Delta^{14}\text{C}_{\text{atm}}$   
60 values over the last 54 kyr. Relatively high  $\Delta^{14}\text{C}_{\text{atm}}$  values continued until ~25 kyr BP, then gradually diminished to  
61 preindustrial levels, interrupted by a sharp drop in  $\Delta^{14}\text{C}_{\text{atm}}$  during Heinrich Stadial 1 (HS1) ~17.4 to 14.6 kyr BP  
62 (sometimes called the "mystery interval"; Broecker and Barker, 2007). While the Laschamp geomagnetic excursion  
63 appears to be responsible for the  $\Delta^{14}\text{C}_{\text{atm}}$  peak at ~41 kyr BP, the production rate estimates during much of the pre-  
64 Holocene period are subject to considerable uncertainty.

65  
66 Paleointensity-based reconstructions are sensitive to coring disturbances of poorly consolidated sediments.  
67 The last 50 kyr are represented by the relatively slushy uppermost few meters of recovered marine sediment cores  
68 (Channell et al., 2018). Channell et al. (2018) preferentially selected cores recovered using conventional piston and  
69 square barrel gravity coring methods, and from sites with high mean ( $> 15 \text{ cm kyr}^{-1}$ ) sedimentation rates, so as to  
70 minimize the influence of drilling disturbance, and reached very different production rates than, e.g., Laj et al. (2000).  
71 On the other hand, ice-core  $^{10}\text{Be}$  records are affected by changes in the transport and deposition of atmospheric  $^{10}\text{Be}$ ,  
72 which may overprint the production rate changes (e.g., Heikkilä et al., 2013). Furthermore, in order to calculate the  
73 ice-core  $^{10}\text{Be}$  deposition fluxes, snow accumulation rates must be known for each specific ice core, which themselves

74 have uncertainties on the order of 10 to 20 percent that propagate into the ice-core  $^{10}\text{Be}$  fluxes (Gkinis et al., 2014;  
75 Rasmussen et al., 2013). The large uncertainties associated with the reconstruction of past changes in  $^{14}\text{C}$  production  
76 hamper our ability to predict reliably the extent to which production changes contributed to high glacial  $\Delta^{14}\text{C}_{\text{atm}}$  levels.  
77 Only if estimates of past changes in  $^{14}\text{C}$  production are robust can one improve assessments of the relative importance  
78 of the two fundamental mechanisms responsible for glacial-interglacial  $\Delta^{14}\text{C}$  changes: (1) production changes and (2)  
79 carbon cycle changes.

80  
81 Earlier model studies have focused heavily on the  $\sim 190$  permil drop in  $\Delta^{14}\text{C}_{\text{atm}}$  during HSI and on the deglacial  
82 trends in  $\Delta^{14}\text{C}_{\text{atm}}$  after HS1 (Muscheler et al., 2004; Broecker and Barker, 2007; Skinner et al., 2010; Mariotti et al.,  
83 2016; Delaygue et al., 2003; Marchal et al., 2001; Huiskamp and Meissner, 2012; Hain et al., 2014). Historically, the  
84 younger portion of the  $\Delta^{14}\text{C}_{\text{atm}}$  record has received more attention than the glacial section because of the early emphasis  
85 on the general climatic trends of the North Atlantic stadials (HS1 and the Younger Dryas [YD]) and the Bølling-  
86 Allerød (BA) warm period, and on the important role of an exceptionally aged ( $^{14}\text{C}$ -depleted) deep-water mass in the  
87 pulsed rise of atmospheric  $\text{CO}_2$  during the last glacial termination (e.g., Skinner et al., 2017). Less research over the  
88 last few decades has studied the specific mechanisms responsible for high glacial  $\Delta^{14}\text{C}_{\text{atm}}$  levels. The model studies  
89 that are available point out the difficulties in simulating the correct glacial  $\Delta^{14}\text{C}_{\text{atm}}$  levels (Hughen et al., 2004; Köhler  
90 et al., 2006). These studies demonstrate with box models that glacial levels of  $\Delta^{14}\text{C}_{\text{atm}}$  cannot be attained without  
91 invoking significant changes in ocean circulation, air-sea gas exchange, and carbonate sedimentation. However, the  
92 box models were not able to reproduce  $\Delta^{14}\text{C}_{\text{atm}}$  values higher than 700 permil, and these results still need to be  
93 scrutinized with models of higher complexity. To our knowledge, no three-dimensional ocean biogeochemical model  
94 has yet simulated the 50,000-year record of  $\Delta^{14}\text{C}_{\text{atm}}$ . Many questions remain unanswered, in particular: What  
95 mechanism can account for the persistence of relatively high  $\Delta^{14}\text{C}_{\text{atm}}$  values during the millennia after the Laschamp  
96 excursion?

97  
98 The expected time scale for sustaining elevated levels of  $\Delta^{14}\text{C}_{\text{atm}}$  after a production peak is on the order of  
99 thousands of years, a time scale tied to the mean lifetime of  $^{14}\text{C}$  ( $\sim 8223$  years; Audi et al., 2003; Bé et al., 2013) and  
100 the time required for deep ocean ventilation (on the order of 1000 years or more; Primeau, 2005). Specifically,  
101 Muscheler et al. (2004) demonstrate that the characteristic time constant for equilibration of  $\Delta^{14}\text{C}_{\text{atm}}$  after a  
102 perturbation in atmospheric production is 5000 years. By this analysis, the Laschamp event, which lasted only about  
103 1500 to 2000 years (Laj et al., 2000), was insufficient to sustain the high  $\Delta^{14}\text{C}_{\text{atm}}$  values observed over the next  $\sim 15,000$   
104 years. The lack of significant changes (only  $\sim 10$  percent) in atmospheric  $\text{CO}_2$  during the time period of interest raises  
105 the question of what causes variations in  $\Delta^{14}\text{C}_{\text{atm}}$ , but not  $\text{CO}_2$ , on millennial time scales? The obvious answers are:  
106 cosmic ray modulation and air-sea gas exchange. Ultimately, no explanation for high glacial  $\Delta^{14}\text{C}_{\text{atm}}$  levels can be  
107 complete in the absence of more robust estimates of the pre-Holocene  $^{14}\text{C}$  production rate, as well as a good  
108 understanding of the ocean carbon cycle under glacial climate conditions.

109

110 One of the major challenges associated with modelling glacial-interglacial climate cycles is that it is currently  
111 not possible to reproduce climate and atmospheric CO<sub>2</sub> variations on the basis of orbital forcing alone. Problems  
112 include the complexity of the Earth system, making it difficult to represent all the relevant processes in models, and  
113 the long time scales involved, making simulations covering tens of thousands of years costly in computation time.  
114 Glacial-interglacial simulations with dynamic ocean and land models of intermediate complexity have begun to  
115 emerge, but these models are not yet able to reproduce the reconstructed variations in important proxy data or the  
116 timing of CO<sub>2</sub> variations during the last glacial termination (Brovkin et al., 2012; Ganopolski and Brovkin, 2017;  
117 Menviel et al., 2012). A wide variety of mechanisms, both physical and biological, centered on or connected with the  
118 ocean, as well as exchange processes with the land biosphere, marine sediments, coral reefs, and the lithosphere, are  
119 thought to play a role in explaining the glacial-interglacial variations in atmospheric CO<sub>2</sub> (Archer et al., 2000; Fischer  
120 et al., 2010; Wallmann et al., 2016; Galbraith and Skinner, 2020), but how they interacted over time under the influence  
121 of orbital forcing remains elusive. We appear to still be missing a single framework in which these mechanisms are  
122 linked to each other in a predictable manner. As long as there are still large gaps in our understanding of the glacial  
123 climate and associated ocean carbon cycle, a convenient way to examine the impact of the possible mechanisms on  
124 atmospheric CO<sub>2</sub> levels, and here on  $\Delta^{14}\text{C}_{\text{atm}}$ , is to perform sensitivity experiments and scenario-based simulations  
125 with models. This allows us to investigate specific phenomena in idealized settings, permitting us to investigate in  
126 detail which parameters and processes are most important in controlling  $\Delta^{14}\text{C}_{\text{atm}}$  levels.

127  
128 In this paper we extend previous modelling efforts concerning the record of  $\Delta^{14}\text{C}_{\text{atm}}$  with respect to three  
129 issues: (1) the sensitivity of the  $\Delta^{14}\text{C}_{\text{atm}}$  response to carbon cycle changes and the potential importance of marine  
130 sediments, (2) the simulation of  $\Delta^{14}\text{C}_{\text{atm}}$  covering the time range of the IntCal13 radiocarbon calibration curve (50,000  
131 years), the primary focus being the explanation of high glacial  $\Delta^{14}\text{C}_{\text{atm}}$  levels, and (3) a new 50,000-year record of the  
132 <sup>14</sup>C production rate, as inferred by deconvolving the reconstructed histories of  $\Delta^{14}\text{C}_{\text{atm}}$  and CO<sub>2</sub> with a prognostic  
133 carbon cycle model and considering the uncertainties associated with the glacial-interglacial ocean carbon cycle. In  
134 the following sections we first introduce the Bern3D earth system model of intermediate complexity and describe the  
135 carbon cycle scenarios for forcing it. We then use step changes in the <sup>14</sup>C production rate and in selected parameters  
136 of the ocean carbon cycle model to gain insight into the transient and equilibrium response of  $\Delta^{14}\text{C}_{\text{atm}}$ . After these  
137 sensitivity experiments we present the results of paleoclimate simulations forced by available reconstructions of past  
138 changes in <sup>14</sup>C production together with reconstructed and hypothetical carbon cycle changes accompanying glacial-  
139 interglacial climate cycles. Finally, we present results for a first attempt to reconstruct the glacial history of the <sup>14</sup>C  
140 production rate using the Bern3D model forced with reconstructed variations in  $\Delta^{14}\text{C}_{\text{atm}}$  and CO<sub>2</sub> as well as a wide  
141 range of carbon cycle scenarios. We end with a comparison of three fundamentally different (model-based,  
142 paleointensity-based, and ice-core <sup>10</sup>Be-based) reconstructions of atmospheric <sup>14</sup>C production.

## 143 144 **2 Materials and methods**

### 145 146 **2.1 Brief description of the Bern3D model**

147  
148 Simulations are performed with the computationally efficient Bern3D earth system model of intermediate complexity  
149 (version 2.0), which is designed for long-term climate simulations over several tens of thousands of years. The Bern3D  
150 couples a frictional geostrophic 3-D ocean general circulation model (Edwards et al., 1998; Edwards and Marsh, 2005;  
151 Müller et al., 2006), a 2-D energy-moisture balance atmosphere model (Ritz et al., 2011), an ocean carbon cycle model  
152 (Müller et al., 2008; Tschumi et al., 2008; Parekh et al., 2008), a chemically active 10-layer ocean sediment model  
153 (Heinze et al., 1999; Tschumi et al., 2011; Roth et al., 2014; Jeltsch-Thömmes et al., 2019), and a four-box model  
154 representing carbon stocks in the terrestrial biosphere (Siegenthaler and Oeschger, 1987). The coarse-resolution ocean  
155 model is implemented on a 41 x 40 horizontal grid, with 32 logarithmically spaced layers in the vertical. The seasonal  
156 cycle is resolved with 96 time steps per year. The tracers carried in the ocean model include temperature, salinity,  
157 dissolved inorganic carbon (DIC), dissolved organic carbon (DOC), carbon isotopes ( $^{14}\text{C}$  and  $^{13}\text{C}$ ) of DIC and DOC,  
158 alkalinity (Alk), phosphate (P), silicate (Si), iron, dissolved oxygen ( $\text{O}_2$ ), preformed dissolved oxygen ( $\text{O}_{2,\text{pre}}$ ), and an  
159 “ideal age” tracer. The ideal age is set to zero in the surface layer, increased by  $\Delta t$  in all interior grid cells at each time  
160 step of duration  $\Delta t$ , and transported by advection, diffusion, and convection. Atmospheric  $\text{CO}_2$ ,  $^{14}\text{CO}_2$ , and  $^{13}\text{CO}_2$  are  
161 also carried as tracers in the atmosphere model. For a more complete description of the Bern3D model, the reader is  
162 referred to Appendix A.

## 163 164 **2.2 Implementation of the $^{14}\text{C}$ tracer**

165  
166 Natural radiocarbon ( $^{14}\text{C}$ ) is a cosmogenic radionuclide produced in the atmosphere by cosmic radiation. Once  
167 oxidized to  $^{14}\text{CO}_2$ , it participates in the global carbon cycle. Atmospheric  $^{14}\text{CO}_2$  invades the ocean by air-sea gas  
168 exchange, where it is subject to the same physical and biogeochemical processes that affect DIC. The only difference  
169 is that  $^{14}\text{C}$  is lost by radioactive decay (half-life of  $5700 \pm 30$  years; Audi et al., 2003; Bé et al., 2013). The governing  
170 natural processes, namely, atmospheric  $^{14}\text{C}$  production, air-sea gas exchange, physical transport and mixing in the  
171 water column, biological production and export of particulate and dissolved matter from the surface ocean, particle  
172 flux through the water column, particle deposition on the sea floor, remineralization and dissolution in the water  
173 column and the sediment pore waters, and vertical sediment advection and sediment accumulation, are explicitly  
174 represented in the Bern3D model (see Fig. 2). Air-sea gas exchange is parameterized using a modified version of the  
175 standard gas transfer formulation of OCMIP-2, with exchange rates that vary across time and space (see Appendix A  
176 for more details).

177  
178 Radiocarbon measurements are generally reported as  $\Delta^{14}\text{C}$ , i.e., the ratio of  $^{14}\text{C}$  to total carbon C relative to  
179 that of the AD 1950 atmosphere, with a correction applied for fractionation effects, e.g., due to gas exchange and  
180 photosynthesis (see Stuiver and Polach, 1977). In this model study,  $\Delta^{14}\text{C}$  is treated as a diagnostic variable using the  
181 two-tracer approach of OCMIP-2. Rather than treating the  $^{14}\text{C}/\text{C}$  ratio as a single tracer, fractionation-corrected  $^{14}\text{C}$  is  
182 carried independently from the carbon tracer. The modelled  $^{14}\text{C}$  concentration is normalized by the standard ratio of  
183 the preindustrial atmosphere ( $^{14}r_{\text{std}} = 1.170 \times 10^{-12}$ ; Orr et al., 2017) in order to minimize the numerical error of

184 carrying very small numbers. For comparison to observations,  $\Delta^{14}\text{C}$  is calculated from the normalized and  
185 fractionation-corrected modelled  $^{14}\text{C}$  concentration as follows:

$$187 \quad \Delta^{14}\text{C} = 1000(^{14}r' - 1) \quad (1)$$

188  
189 where  $^{14}r'$  is the ratio of  $^{14}\text{C}/\text{C}$  in either atmospheric  $\text{CO}_2$  or oceanic DIC divided by  $^{14}r_{std}$ , depending on the reservoir  
190 being considered. The approach taken to simulate atmospheric  $^{14}\text{CO}_2$  is analogous to the approach used for  $\text{CO}_2$ ,  
191 except that the equation includes the terms due to atmospheric production and radioactive decay. For simulations  
192 where the sediment model is active, the oceanic DIC tracer sees a constant input from terrestrial weathering, whereas  
193 there is no weathering input of  $\text{DI}^{14}\text{C}$  to the ocean (see Appendix A for more details).

194  
195 In the preindustrial spin-up simulation needed to initialize the Bern3D model, atmospheric  $\text{CO}_2$  is held  
196 constant at 278.05 ppm and  $\Delta^{14}\text{C}_{\text{atm}}$  at 0 permil. During this integration time the ocean inventories of carbon and  $^{14}\text{C}$   
197 adjust to the forcing fields. The resulting changes after >50,000 years of integration are negligibly small. Fig. 3 shows  
198 the steady-state  $\Delta^{14}\text{C}$  distribution in the surface (< 100 m) and deep (> 1500 m) ocean for the preindustrial control run.  
199 The large-scale distribution of modelled oceanic  $\Delta^{14}\text{C}$  broadly resembles the observed pattern in the Global Ocean  
200 Data Analysis Project (GLODAP; Key et al., 2004). That final state (i.e., the end of the preindustrial spin-up) is used  
201 to diagnose the  $^{14}\text{C}$  production rate for the preindustrial atmosphere, such that the rate of  $^{14}\text{C}$  production is balanced  
202 by radioactive decay and the net fluxes out of the atmosphere. For transient simulations, an adjustable scale factor is  
203 applied to the preindustrial steady-state value of 443.9 mol  $^{14}\text{C}$  per year ( $1.66 \text{ atoms cm}^{-2} \text{ s}^{-1}$ ) in order to account for  
204 production changes induced by solar and/or geomagnetic modulation. These production changes are derived from,  
205 e.g., available reconstructions of the  $^{14}\text{C}$  production rate in relative units, as detailed in Sect. 2.5. Note the preindustrial  
206 spin-up results in steady-state values for weathering-derived inputs of DIC, Alk, P, and Si of 0.46 Gt C per year, 34.37  
207 Tmol Alk per year, 0.17 Tmol P per year, and 6.67 Tmol Si per year, respectively. These terrestrial weathering rates  
208 were chosen to balance the sedimentation rates on the sea floor and are held fixed and constant throughout the  
209 simulations.

### 210 211 **2.3 Model configurations**

212  
213 We focus in this paper on the response of  $\Delta^{14}\text{C}_{\text{atm}}$  to changes in  $^{14}\text{C}$  production and the ocean carbon cycle. For a  
214 deeper mechanistic understanding of the driving processes, step response experiments are first performed (see Sect.  
215 3.1). These simulations include perturbations of the steady-state  $^{14}\text{C}/\text{C}$  distribution under preindustrial conditions. We  
216 investigate the impact of step changes in (1) the  $^{14}\text{C}$  production rate (“higher production” scenario), (2) wind stress  
217 and vertical diffusivity (“reduced deep ocean ventilation” scenario), and (3) the gas transfer velocity (“enhanced  
218 permanent sea ice cover” scenario). After a step change at time 0, the simulations are run to near-equilibrium over a  
219 50,000-year integration. The following model configurations and therefore exchanging carbon reservoirs are

220 considered: atmosphere–ocean (OCN), atmosphere–ocean–land (OCN-LND), atmosphere–ocean–sediment (OCN-  
221 SED), and atmosphere–ocean–land–sediment (ALL).

222

223 Next we examine the influence of changes that are transient in nature. We simulate  $\Delta^{14}\text{C}_{\text{atm}}$  over the full range  
224 of the  $^{14}\text{C}$  dating method (i.e., 50 to 0 kyr BP) (see Sect. 3.2 and 3.3). These transient simulations are initialized at 70  
225 kyr BP using model configuration ALL, and forced by reconstructed changes in  $^{14}\text{C}$  production (see Sect. 2.5) over a  
226 70,000-year integration. The first 20,000 years of the integration are considered a spin-up. Although the full record is  
227 simulated, we focus our analysis on the millennial-scale variation in  $\Delta^{14}\text{C}_{\text{atm}}$  before incipient deglaciation at  $\sim 18$  kyr  
228 BP. Eight model runs are carried out for each production rate reconstruction, using different combinations of forcing  
229 fields and parameter values as described next.

230

## 231 **2.4 Carbon cycle scenarios**

232

233 In our transient simulations with the Bern3D model, eight scenarios based on different assumptions about the global  
234 carbon cycle are considered, the details of which are summarized in Table 1. The goal is to investigate the extent to  
235 which changes in the ocean carbon cycle could explain high glacial  $\Delta^{14}\text{C}_{\text{atm}}$  levels, given available reconstructions of  
236 past changes in  $^{14}\text{C}$  production. We therefore consider a wide range of carbon cycle scenarios, including some extreme  
237 cases. A note of caution. Because millennial-scale  $\Delta^{14}\text{C}_{\text{atm}}$  variations during the last glacial are what we are interested  
238 in, we do not attempt to reproduce abrupt climate perturbations such as Dansgaard-Oeschger warming events in the  
239 model runs.

240

241 In the first scenario (MOD), the model is run with fixed preindustrial boundary conditions for the Earth’s  
242 orbital parameters, radiative forcing due to well-mixed greenhouse gases, and ice sheet extent. As a consequence,  
243 atmospheric  $\text{CO}_2$  remains approximately constant at the preindustrial level of 278.05 ppm over the simulation. The  
244 second scenario (PAL) considers reasonably well-known climate forcing over the last glacial-interglacial cycle.  
245 Simulations under this scenario are initialized with output from a previous spin-up simulation forced by glacial  
246 boundary conditions with respect to orbital parameters (Berger, 1978), ice sheet extent (see below), and greenhouse  
247 gas radiative forcing based on the smoothed dataset of atmospheric greenhouse gases by Köhler et al. (2017) as  
248 constructed from the original data of Ahn and Brook (2014), Ahn et al. (2012), Bauska et al. (2015), Bereiter et al.  
249 (2012), Buizert et al. (2015), Dlugokencky et al. (2016), Laurantou et al. (2010), Lüthi et al. (2010), MacFarling-  
250 Meure et al. (2006), Marcott et al. (2014), Monnin et al. (2001, 2004), Rubino et al. (2013), Schneider et al. (2013),  
251 and Sigl et al. (2016). In simulations under PAL, the model is integrated until 0 kyr BP following the reconstructed  
252 histories of orbital forcing, ice sheets, and radiative forcing due to greenhouse gases. Ice sheets for the preindustrial  
253 and Last Glacial Maximum (LGM) states are taken from Peltier (1994) and linearly scaled using the global benthic  
254  $\delta^{18}\text{O}$  stack of Lisiecki and Stern (2016), which is a global ice volume proxy. Changes in the albedo, salinity and latent  
255 heat flux associated with the ice sheet buildup or melting are also taken into account (Ritz et al., 2011). Note that,

256 although the radiative forcing for CO<sub>2</sub> is prescribed, the atmospheric CO<sub>2</sub> concentration is allowed to evolve freely,  
257 except in the simulations described in Sect. 2.5.

258

259 Model scenario PAL appears to still be missing an important process or feedback for atmospheric CO<sub>2</sub>, as it  
260 cannot reproduce the observed low glacial CO<sub>2</sub> level without invoking additional changes (see, e.g., Tschumi et al.,  
261 2011; Menviel et al., 2012; Roth and Joos, 2013; Jeltsch-Thömmes et al., 2019). Variations in atmospheric CO<sub>2</sub> govern  
262 how fast  $\Delta^{14}\text{C}$  signatures are passed between the atmosphere and ocean. Gross fluxes of <sup>14</sup>C between the atmosphere  
263 and ocean, and vice versa, scale with atmospheric pCO<sub>2</sub> and its <sup>14</sup>C/C ratio. It is therefore important to reproduce low  
264 glacial atmospheric CO<sub>2</sub> concentrations in at least some of the model scenarios, thereby capturing the influence of  
265 temporal changes in CO<sub>2</sub> on the air-sea exchange of <sup>14</sup>C. In this study, we consider six scenarios that invoke additional  
266 changes to force the model toward the observed low glacial CO<sub>2</sub> concentration. In addition to the PAL forcing, a time-  
267 varying scale factor  $F(t)$  is applied to some combination of tunable model parameters: wind stress scale factor  $\tau$ ,  
268 vertical diffusivity  $K_V$ , gas transfer velocity  $k_w$ , CaCO<sub>3</sub>-to-particulate organic carbon (POC) export ratio  $rr$ , and POC  
269 remineralization length scale  $\ell_{POC}$ . For the preindustrial period, the value of  $F(t)$  is fixed at 1, whereas the theoretical  
270 LGM value was chosen in order to achieve an atmospheric CO<sub>2</sub> concentration close to the LGM level of ~190 ppm  
271 (see Table 1), as determined by sensitivity experiments. Note that the same values of  $F(t)$  apply to any of the model  
272 parameters considered in a given scenario. To obtain intermediate values,  $F(t)$  is linearly scaled using the global  
273 benthic  $\delta^{18}\text{O}$  stack (see Fig. 1). For the spin-up needed to initialize these simulations, the glacial spin-up simulation  
274 of PAL was integrated for 50,000 model years, with tunable parameters adjusted to their appropriate glacial values.  
275 Atmospheric CO<sub>2</sub> drawdown of up to ~100 ppm is achieved over this 50,000-year integration. From that final spun-  
276 up state, the model is run forward in time until 0 kyr BP with PAL and  $F(t)$  forcing.

277

278 The first of these scenarios (CIRC) allows us to test the sensitivity of the model results with respect to changes  
279 in ocean circulation. Tunable model parameters  $\tau$  and  $K_V$  were reduced to 40 percent of their preindustrial values  
280 throughout the global ocean during the LGM (i.e.,  $F_{\tau, K_V} = 0.4$ ). Such a drastic change in the wind stress field is not  
281 realistic. Rather, these changes should be viewed as “tuning knobs” that force the ocean model into a poorly ventilated  
282 state with an “older” ideal age and <sup>14</sup>C-depleted deep waters, as suggested for the glacial ocean (e.g., Sarnthein et al.,  
283 2013; Skinner et al., 2017). In the model’s implementation, a change in wind stress does not affect the gas transfer  
284 velocity  $k_w$ , unlike in the real ocean where changes in wind stress and wind speed act together. The influence of a  
285 change in air-sea exchange efficiency on the model results was investigated in a second scenario (VENT) where  $k_w$   
286 is reduced in the model’s north (> 60°N) and south (> 48°S) polar areas in addition to global reductions of  $\tau$  and  $K_V$   
287 ( $F_{\tau, K_V, k_w} = 0.4$ ). A 60 percent reduction of  $k_w$  is unlikely to be correct but is a straightforward way to reduce the  
288 model’s gas exchange efficiency. In the third scenario (VENTx), reduction of polar  $k_w$  to 0 percent of its preindustrial  
289 value was tested ( $F_{\tau, K_V} = 0.4$ ;  $F_{k_w} = 0.0$ ). Here,  $k_w$  remains fixed at 0 percent during the last glacial and is adjusted  
290 to its preindustrial value via a linear ramp across the last glacial termination (~18 to 11 kyr BP). In this scenario, sea  
291 ice would permanently cover 100 percent of the Southern Ocean during the last glacial, which is not supported by the



292 sea ice reconstructions of Gersonde et al. (2005) and Allen et al. (2011), and also the high-latitude ( $> 60^\circ\text{N}$ ) North  
293 Atlantic and Arctic Ocean, for which there is some evidence (Müller and Stein, 2014; Hoff et al., 2016).

294

295 We end by investigating the sensitivity of the model results to changes in the parameters controlling the  
296 export production of  $\text{CaCO}_3$  and the water column remineralization of POC. Model scenario BIO considers changes  
297 of the  $\text{CaCO}_3$ -to-POC export ratio (and thus also the  $\text{CaCO}_3$ -to-POC rain ratio; Archer and Maier-Reimer, 1994)  
298 ( $F_{rr} = 0.8$ ) and POC remineralization length scale (Roth et al., 2014) ( $F_{\ell_{POC}} = 1.2$ ). These changes impact the global  
299 carbon cycle by influencing the vertical gradients of DIC, Alk, and nutrients in the water column. A change in the  
300 fluxes of POC and  $\text{CaCO}_3$  to the sea floor drives a change in the magnitude of their removal by sedimentation on the  
301 sea floor. A modest reduction in the export ratio during the last glacial is compatible with reconstructed variations in  
302 carbonate ion concentrations (Jeltsch-Thömmes et al., 2019). How the depth of POC remineralization changed over  
303 time is still unknown. The last two scenarios consider the combined effect of physical and biogeochemical changes:  
304 PHYS-BIO ( $F_{\tau,K_V,k_w,rr} = 0.7$ ) and PHYS-BIOx ( $F_{\tau,K_V,k_w,rr} = 0.8$ ;  $F_{\ell_{POC}} = 1.2$ ).

305

## 306 2.5 Measurement- and model-based reconstruction of $^{14}\text{C}$ production

307

308 Our ability to attribute past changes in  $\Delta^{14}\text{C}_{\text{atm}}$  to climate-related changes in the ocean carbon cycle is limited by our  
309 ability to reconstruct a precise and accurate history of the  $^{14}\text{C}$  production rate. Past changes in  $^{14}\text{C}$  production can be  
310 estimated from geomagnetic field reconstructions and from  $^{10}\text{Be}$  measurements in polar ice cores. For ice-core  $^{10}\text{Be}$ -  
311 based estimates, we use the ice-core radionuclide stack of Adolphi et al. (2018), which is based on  $^{36}\text{Cl}$  data from the  
312 GRIP ice core (Baumgartner et al., 1998), and on  $^{10}\text{Be}$  data from the GRIP (Yiou et al., 1997; Baumgartner et al.,  
313 1997; Wagner et al., 2001; Muscheler et al., 2004; Adolphi et al., 2014) and GISP2 (Finkel and Nishiizumi, 1997) ice  
314 cores. It also includes  $^{10}\text{Be}$  data from the NGRIP, EDML, EDC, and Vostok ice cores around the Laschamp  
315 geomagnetic excursion (Raisbeck et al., 2017). It has been extended to the present using the  $^{10}\text{Be}$  stack of Muscheler  
316 et al. (2016). All ice cores were first placed on the same time scale (GICC05) before  $^{10}\text{Be}$  fluxes were calculated. This  
317 70,000-year  $^{10}\text{Be}$  stack provides relative changes of  $^{14}\text{C}$  production rates under the assumption that  $^{14}\text{C}$  and  $^{10}\text{Be}$   
318 production rates are directly proportional, as indicated by the most recent production rate models (e.g., Herbst et al.,  
319 2017).

320

321 For paleointensity-based estimates, we employ (1) the North Atlantic Paleointensity Stack, or NAPIS, by Laj  
322 et al. (2000) as extended by Laj et al. (2002), (2) the Global Paleointensity Stack, or GLOPIS, by Laj et al. (2004), (3)  
323 a high-resolution paleointensity stack from the Black Sea (Nowaczyk et al., 2013), and (4) a paleointensity stack from  
324 Iberian Margin sediments (Channell et al., 2018). In principle, stacks of widely distributed cores (NAPIS/GLOPIS)  
325 are expected to yield a better representation of the global geomagnetic dipole moment, whereas the paleointensity  
326 stacks from the Black Sea and the Iberian Margin avoid some of the problems associated with coring disturbances.  
327 The four different paleointensity stacks were converted to  $^{14}\text{C}$  production rates using the production rate model of

328 Herbst et al. (2017), the local interstellar spectrum of Potgieter et al. (2014), and assuming a constant solar modulation  
329 potential of 630 MeV.

330

331 An alternative approach to estimating the  $^{14}\text{C}$  production rate is to combine an atmospheric radiocarbon  
332 budget with a prognostic carbon cycle model. Here simulations are performed with the Bern3D model and forced by  
333 reconstructed changes in  $\Delta^{14}\text{C}_{\text{atm}}$  and  $\text{CO}_2$ , as well as reconstructed and hypothetical carbon cycle changes, over the  
334 last 50 kyr. Both the IntCal13 calibration curve (Reimer et al., 2013) and the recent Hulu Cave  $\Delta^{14}\text{C}_{\text{atm}}$  dataset (Cheng  
335 et al., 2018) are used. Note that although the forthcoming IntCal20 calibration curve (Reimer et al., in press) will be  
336 the new standard atmospheric radiocarbon record for the last 55,000 years, essentially all data underlying IntCal20  
337 before 13.9 kyr BP are tied to the Hulu Cave dataset, either via time scales (Lake Suigetsu plant macrofossil data) or  
338 marine reservoir corrections (marine records). Hence, the IntCal20 and Hulu Cave  $\Delta^{14}\text{C}_{\text{atm}}$  records are very similar  
339 and using IntCal20 would not impact our conclusions.

340

341 The  $^{14}\text{C}$  production rate  $Q$  is calculated, each model year, from the air-sea  $^{14}\text{CO}_2$  flux ( $F_{as}$ ), the atmosphere-  
342 land  $^{14}\text{CO}_2$  flux ( $F_{ab}$ ), the loss of  $^{14}\text{C}$  due to radioactive decay, and the change ( $\dot{I}_a$ ) in the atmospheric  $^{14}\text{C}$  inventory  
343 ( $I_a$ ):

344

$$345 \quad Q = F_{as} + F_{ab} + \lambda I_a + \dot{I}_a \quad (2)$$

346

347 where  $\lambda$  is the radioactive decay constant for  $^{14}\text{C}$ , i.e.,  $\lambda = \ln 2 / 5700 \text{ years} = 1.2160 \times 10^{-4} \text{ yr}^{-1}$ . The radioactive decay  
348 term  $\lambda I_a$  and the change in inventory  $\dot{I}_a$  follow the reconstructed  $\Delta^{14}\text{C}_{\text{atm}}$  and  $\text{CO}_2$  records, whereas  $F_{as}$  and  $F_{ab}$  are  
349 explicitly computed by the model. The  $F_{as}$  term depends strongly on the carbon cycle scenario under consideration  
350 (see Sect. 2.4 and Table 1). For comparison with other reconstructions,  $Q$  is converted into a relative value by  
351 normalizing it by the preindustrial value.

352

### 353 **3 Results and discussion**

354

#### 355 **3.1 Atmospheric $\Delta^{14}\text{C}$ response to step changes**

356

357 We use step changes in the  $^{14}\text{C}$  production rate, and in selected carbon cycle parameters, to gain insight into the  
358 characteristic magnitude and time scale of the corresponding  $\Delta^{14}\text{C}_{\text{atm}}$  changes (Fig. 4). Besides variations of the  
359 production rate, changes in ocean circulation and air-sea gas exchange are considered the most important factors  
360 affecting  $\Delta^{14}\text{C}_{\text{atm}}$ . Their effect on  $\Delta^{14}\text{C}_{\text{atm}}$  can be understood in terms of their effect on the reservoir sizes involved in  
361 the global carbon cycle and on the exchange rates between the reservoirs. We investigate the relative importance of  
362 the major global carbon reservoirs (atmosphere, terrestrial biosphere, ocean, and sediments) by considering four  
363 different model configurations (see Sect. 2.3), with particular emphasis on the role of marine sediments.

364

365 In model studies, the process of sedimentation (defined here as the difference between deposition and  
366 remineralization/dissolution of material on the sea floor) is often neglected because it is a relatively minor flux. In the  
367 Bern3D model, sedimentation removes only about 0.46 Gt C and 45.31 mol  $^{14}\text{C}$  per year in the preindustrial steady  
368 state. Indeed, the interaction with the ocean sediments has little influence on the global mean value of oceanic  $\Delta^{14}\text{C}$   
369 and therefore  $\Delta^{14}\text{C}_{\text{atm}}$ , as long as the total oceanic amount of carbon remains approximately constant (Siegenthaler et  
370 al., 1980); however, this is not always true, particularly in the case of millennial-scale climate perturbations. This is  
371 demonstrated by the differences between the model runs with and without sediments (i.e., ALL versus OCN-LND,  
372 and OCN-SED versus OCN) as shown in Fig. 4. The response of  $\Delta^{14}\text{C}_{\text{atm}}$  to various perturbations depends on the  
373 magnitude of the change in the ocean carbon inventory, with a larger change achieved by considering the interaction  
374 with the ocean sediments and the imbalance between weathering and sedimentation (see Fig. 5e,f). In order to facilitate  
375 our discussion, we will make only direct comparisons between model runs ALL and OCN-LND, which both include  
376 the four-box terrestrial biosphere model. We note that the  $^{14}\text{C}$  exchange rate between the atmosphere and the terrestrial  
377 biosphere is only of minor importance for long time scales of millennia and more.

378

### 379 **3.1.1 Change of $^{14}\text{C}$ production**

380

381 At steady state, the relative change of  $\Delta^{14}\text{C}_{\text{atm}}$  is equal to the relative change of the  $^{14}\text{C}$  production rate, irrespective of  
382 the individual reservoirs considered. Fig. 4 shows that  $\Delta^{14}\text{C}_{\text{atm}}$  increases by about 100 permil (or 10 percent) when the  
383 production rate is increased by 10 percent. In model run ALL,  $\Delta^{14}\text{C}_{\text{atm}}$  increases approximately exponentially to its  
384 new steady-state value with a characteristic time constant  $T$  of about 6170 years (i.e.,  $1 - 1/e \approx 63$  percent of the  
385 total change in  $\Delta^{14}\text{C}_{\text{atm}}$  occurs within 6170 years). This e-folding time scale is close to the mean lifetime of  $^{14}\text{C}$  (~8223  
386 years), which is modulated by the time required for  $\Delta^{14}\text{C}$  to equilibrate between the atmosphere and the ocean (i.e.,  
387 the time scale for deep ocean ventilation, of the order of hundreds of years to 1000 years or more). In the next section,  
388 we will investigate the effect of ocean carbon cycle processes on  $\Delta^{14}\text{C}_{\text{atm}}$ .

389

390 Note that for simplicity, we investigated only step changes in atmospheric production, although, in reality,  
391  $^{14}\text{C}$  production varies continuously over time due to changes in the solar and/or geomagnetic modulation of the cosmic  
392 radiation. This results in a non-steady state value of  $\Delta^{14}\text{C}_{\text{atm}}$ .

393

### 394 **3.1.2 Change of ocean circulation**

395

396 The exchange rate between the surface and deep ocean is mainly determined by physical transport and mixing  
397 processes. The overall effect of these processes is to transport  $^{14}\text{C}$ -enriched surface waters to the thermocline and deep  
398 ocean, where waters are typically  $^{14}\text{C}$ -depleted. In addition, the nutrient supply by transport and mixing plays an  
399 important role in determining the production and export of biogenic material from the surface ocean, constituting a  
400 second pathway for transporting  $^{14}\text{C}$  to the deep ocean.

401

402 In the Bern3D model, the tunable model parameters affecting the ventilation of the deep ocean include a  
403 scale factor  $\tau$  for the wind stress field and vertical diffusivity  $K_V$ . Fig. 4 shows the  $\Delta^{14}\text{C}_{\text{atm}}$  response after a sudden  
404 decrease of  $\tau$  and  $K_V$  by 50 percent. Although a halving of  $\tau$  and  $K_V$  does not represent a realistic change, the resulting  
405 state of the ocean's large-scale overturning circulation can be interpreted in terms of the "ideal age" of water, which  
406 represents the average time since a water mass last made surface boundary contact. The new steady-state ideal age  
407 after a halving of  $\tau$  and  $K_V$  is almost three times greater than the preindustrial steady-state value (i.e., ~1664 years  
408 versus ~613 years). This "ageing" of the ocean is achieved through a weakening and shoaling of the global meridional  
409 overturning circulation as evident from a moderate reduction in the meridional overturning stream function for the  
410 Indo-Pacific Ocean from about 14 to 9.5 Sv (1 Sv =  $10^6 \text{ m}^3 \text{ s}^{-1}$ ), and a very strong reduction from about 18 to 8 Sv in  
411 the Atlantic meridional overturning stream function, consistent with evidence for the glacial ocean. Here, as expected,  
412 the overall effect of deep water ageing is a stronger vertical  $\Delta^{14}\text{C}$  gradient in the water column and a subsequent  
413 increase in  $\Delta^{14}\text{C}_{\text{atm}}$ . The exact nature of the  $\Delta^{14}\text{C}_{\text{atm}}$  response, however, depends on the carbon reservoirs considered.  
414

415 If the ocean sediment reservoir is neglected, the time required for  $\Delta^{14}\text{C}_{\text{atm}}$  to adjust to step changes in  $\tau$  and  
416  $K_V$  is relatively short.  $\Delta^{14}\text{C}_{\text{atm}}$  increases rapidly to its new steady-state value of ~159 permil, with a time constant T of  
417 about 600 years. This increase of  $\Delta^{14}\text{C}_{\text{atm}}$  can be explained by the fact that, owing to a weaker and shallower  
418 overturning circulation, a comparatively large amount of carbon is moved from the atmosphere to the ocean. More  
419 specifically, the atmospheric carbon inventory decreases by 14.6 percent, whereas the atmospheric  $^{14}\text{C}$  inventory  
420 decreases by only 1.1 percent (Fig. 5c). The  $^{14}\text{C}$  being produced in the atmosphere is therefore diluted by a smaller  
421 carbon inventory, increasing the atmospheric  $^{14}\text{C}/\text{C}$  ratio; this asymmetry in the drawdown of  $\text{CO}_2$  and  $^{14}\text{CO}_2$  is what  
422 permits the increase of  $\Delta^{14}\text{C}_{\text{atm}}$ . Since the ocean carbon inventory changes by only +0.2 percent, the mean  $\Delta^{14}\text{C}$  value  
423 for the global ocean is nearly unaffected, a decrease of only ~11 permil in the new steady state (Fig. 6g).  
424

425 In the model run where the sediment model is active, there are two distinct time constants. A rapid increase  
426 of  $\Delta^{14}\text{C}_{\text{atm}}$  occurs, ~143 permil in the first few hundred years, then  $\Delta^{14}\text{C}_{\text{atm}}$  gradually decreases to its final value of ~91  
427 permil after tens of thousands of years. Reduced deep ocean ventilation is again responsible for the rapid  $\Delta^{14}\text{C}_{\text{atm}}$   
428 change and the respective time constant (T = ~480 years). The second time constant of ~23,390 years is due to the  
429 relatively long time required for the ocean carbon inventory to adjust to the ocean circulation-driven imbalance  
430 between weathering and sedimentation.  
431

432 The process of ocean circulation interacts with the efficiency of the ocean's biological carbon pump, via its  
433 impact on export production, ocean interior oxygen levels, and seawater carbonate chemistry/equilibria. This has  
434 important implications for the sedimentation of biogenic material on the sea floor and, on a time scale of tens of  
435 thousands of years, the total oceanic amount of carbon. Through this coupling of ocean circulation and sea floor  
436 sedimentation via the biological carbon pump, a halving of  $\tau$  and  $K_V$  leads to a 9.8 percent increase of the ocean carbon  
437 inventory in the new steady state (Fig. 5e). Qualitatively, a reduction in the ocean's overturning circulation leads to a  
438 lower surface nutrient supply, which limits the production and export of biogenic material from the surface ocean.

439 This, in turn, decreases the fluxes of POC and CaCO<sub>3</sub> to the sea floor, with major consequences for the magnitude of  
440 their removal by sedimentation. At the same time, a constant input of DIC, Alk, and nutrients is added to the ocean  
441 from terrestrial weathering which is no longer balanced by sedimentation on the sea floor (this is what permits a larger  
442 ocean carbon inventory). The overall effect is a gradual reduction of oceanic  $\Delta^{14}\text{C}$  by  $\sim 76$  permil (Fig. 6g), which  
443 dilutes the initial  $\Delta^{14}\text{C}_{\text{atm}}$  peak by 52 permil.

444

### 445 3.1.3 Change of gas transfer velocity

446

447 It takes about a decade for the isotopic ratios of carbon to equilibrate between the atmosphere and a  $\sim 75$ -m thick  
448 surface mixed layer by air-sea gas exchange (Broecker and Peng, 1974). A consequence of this is that the surface  
449 ocean is undersaturated with respect to  $\Delta^{14}\text{C}_{\text{atm}}$  (see Fig. 3). The choice of gas transfer velocity  $k_w$  as a function of  
450 wind speed is critical for the efficiency of air-sea gas exchange. A reduction of  $k_w$  corresponds to a higher resistance  
451 for gas transfer across the air-sea interface, which means that the  $^{14}\text{C}$  produced in the atmosphere escapes into the  
452 surface ocean at a slower rate. The effect of a lower  $k_w$  is a larger air-sea gradient of  $\Delta^{14}\text{C}$  and higher  $\Delta^{14}\text{C}_{\text{atm}}$  values.  
453 In contrast, the  $\Delta^{14}\text{C}$  value for the surface ocean is nearly unaffected so long as the ocean carbon inventory remains  
454 approximately constant, since the vertical gradient of  $\Delta^{14}\text{C}$  in the ocean is dominated by physical transport and mixing  
455 processes. Although the exact nature of the gas transfer velocity under glacial climate conditions remains unclear,  $k_w$   
456 represents a straightforward way to reduce the model's air-sea exchange efficiency due to theoretical changes in wind  
457 stress, sea ice, etc.

458

459 Fig. 4 shows how  $\Delta^{14}\text{C}_{\text{atm}}$  responds to a perturbation in the gas transfer velocity. In the model run without  
460 sediments, reduction of  $k_w$  to 0 percent of its preindustrial value, in the model's north ( $> 60^\circ\text{N}$ ) and south ( $> 48^\circ\text{S}$ )  
461 polar areas, leads to a moderate increase of  $\Delta^{14}\text{C}_{\text{atm}}$  in the new steady state. The amplitude of  $\Delta^{14}\text{C}_{\text{atm}}$  change is  $\sim 42$   
462 permil, which is achieved with an e-folding time scale  $T$  of about 180 years. This relatively short time constant can be  
463 explained by the multidecadal time scale required for  $\Delta^{14}\text{C}$  to equilibrate between the model's atmosphere, upper  
464 ocean, and terrestrial biosphere. As shown in Fig. 6, the mean  $\Delta^{14}\text{C}$  values for the surface, deep, and global ocean in  
465 the new steady state are only slightly different from the preindustrial steady-state values, as expected from the fact  
466 that the ocean carbon inventory remains relatively stable.

467

468 Interestingly, if sediments are included in the model, the final value of  $\Delta^{14}\text{C}_{\text{atm}}$  is much higher ( $\sim 91$  permil).  
469 In this case, a perturbation in  $k_w$  leads to a very rapid initial increase of  $\Delta^{14}\text{C}_{\text{atm}}$  ( $\sim 42$  permil), and a much slower  
470 subsequent increase of  $\Delta^{14}\text{C}_{\text{atm}}$  ( $\sim 49$  permil). The latter has an e-folding time scale  $T$  of about 14,200 years. This slow  
471 doubling of the initial  $\Delta^{14}\text{C}_{\text{atm}}$  increase is unexpected, but can be explained by the fact that a reduction of  $k_w$  involves  
472 also a reduction of air-sea O<sub>2</sub> gas exchange in the deep water formation regions, decreasing the oceanic oxygen that  
473 is available for transport to the deep ocean. This, in turn, implies lower oxygen concentrations in the water column  
474 and the sediment pore waters, decreasing the rate of POC remineralization in the sediments. Reducing this has the  
475 overall effect of enhancing POC sedimentation on the sea floor, causing the ocean carbon inventory to decrease. As

476 shown in Fig. 5f, the total oceanic amount of carbon decreases by 5.9 percent in the new steady state, resulting in  
477 elevated  $\Delta^{14}\text{C}$  values for the surface (+56 permil), deep (+30 permil), and global (+37 permil) ocean as well as for the  
478 atmosphere (+91 permil) (see Fig. 6). Note that the increase in  $\Delta^{14}\text{C}_{\text{atm}}$  is not accompanied by a significant change in  
479 the atmospheric carbon inventory, which decreases by only 2.2 to 3.3 percent. The air-sea equilibration time scale for  
480  $\text{CO}_2$  by gas exchange is about 1 year for a  $\sim 75$ -m thick surface mixed layer (Broecker and Peng, 1974), which is much  
481 smaller than the ventilation time scale for the deep ocean (on the order of several hundred years or more). One would  
482 therefore expect that the oceanic uptake of  $\text{CO}_2$  demonstrates only a very small response to changes in  $k_w$ .

483

484 Overall, findings from these sensitivity experiments demonstrate that (1) the response of  $\Delta^{14}\text{C}_{\text{atm}}$  to changes  
485 in the internal parameters of the ocean carbon cycle, in contrast to  $^{14}\text{C}$  production changes, depends strongly on  
486 whether or not the balance between terrestrial weathering and sedimentation on the sea floor is simulated, (2) the e-  
487 folding time scale for the initial adjustment of  $\Delta^{14}\text{C}_{\text{atm}}$  to ocean carbon cycle changes, i.e., changes in ocean circulation  
488 and gas exchange, is shorter than that for production changes (i.e.,  $\sim 600$  years and  $\sim 180$  years versus  $\sim 6170$  years),  
489 (3) air-sea gas exchange, in contrast to ocean circulation, has only a small effect on atmospheric  $\text{CO}_2$ , given that gas  
490 exchange is not the rate-limiting step for oceanic  $\text{CO}_2$  uptake, and (4) on time scales of tens of thousands of years  
491 changes in the balance between weathering and sedimentation can potentially diminish (or elevate) the  $\Delta^{14}\text{C}_{\text{atm}}$  value.  
492 This is new, important information for future paleoclimate simulations and suggests that changes in  $\Delta^{14}\text{C}_{\text{atm}}$  may be  
493 overestimated (or underestimated) in models that do not simulate the interaction between sea floor sediments and the  
494 overlying water column.

495

### 496 3.2 Role of $^{14}\text{C}$ production in past atmospheric $\Delta^{14}\text{C}$ variability

497

498 We now consider the component of past  $\Delta^{14}\text{C}_{\text{atm}}$  variability caused by production changes alone. Fig. 7 shows the  
499 results of model runs using different reconstructions of the  $^{14}\text{C}$  production rate, as inferred from paleointensity data  
500 and from ice-core  $^{10}\text{Be}$  fluxes. The global carbon cycle is assumed to be constant and under preindustrial conditions  
501 for these simulations (i.e., scenario MOD is used). Our analysis is restricted to the glacial portion of the record (50 to  
502 18 kyr BP), in part because this is the time period which experiences the largest production changes, and in part  
503 because we did not attempt to reproduce the  $\sim 80$  ppm change in atmospheric  $\text{CO}_2$  that occurred during the last glacial  
504 termination. As we have already noted, much research over the last decades has attempted to explain the observed  
505 glacial-interglacial variations in  $\Delta^{14}\text{C}_{\text{atm}}$  and  $\text{CO}_2$ , and this was not the goal of this study.

506

507 At first glance, the millennial-scale structure of model-simulated  $\Delta^{14}\text{C}_{\text{atm}}$  is comparable to that of the  
508 reconstructions. These similarities appear to be highest for the oldest portion of the record, roughly before 30 kyr BP.  
509 The model reproduces major features of the reconstructed  $\Delta^{14}\text{C}_{\text{atm}}$  variability such as the large changes associated with  
510 the Laschamp ( $\sim 41$  kyr BP) and Mono Lake ( $\sim 34$  kyr BP) geomagnetic excursions. These two events are clearly  
511 expressed as distinct maxima in all model-simulated records. A more detailed comparison reveals a high correlation  
512 between the modelled and reconstructed  $\Delta^{14}\text{C}_{\text{atm}}$  values between 50 and 33 kyr BP. Of note is the better agreement

513 with the new Hulu Cave  $\Delta^{14}\text{C}_{\text{atm}}$  dataset as compared to the IntCal13 calibration curve (i.e., Pearson correlation  
514 coefficient  $r$  of 0.96 versus 0.91). This is likely due to the fact that the Laschamp excursion is smoothed/smeared out  
515 during the stacking process of the IntCal13  $\Delta^{14}\text{C}_{\text{atm}}$  datasets (Adolphi et al., 2018). The correlation between modelled  
516 and reconstructed  $\Delta^{14}\text{C}_{\text{atm}}$  is much weaker during the millennia after the Mono Lake excursion (33 to 18 kyr BP;  $r =$   
517 0.52 to 0.64). While it is clear that much of the millennial-scale variation in  $\Delta^{14}\text{C}_{\text{atm}}$  is driven by past changes in  $^{14}\text{C}$   
518 production, the model fails to reproduce the glacial level of  $\Delta^{14}\text{C}_{\text{atm}}$  and also does not capture the  $\sim 15,000$ -year  
519 persistent elevation of  $\Delta^{14}\text{C}_{\text{atm}}$  or the subsequent decrease of  $\Delta^{14}\text{C}_{\text{atm}}$  after  $\sim 25$  kyr BP.

520

521 The reconstructions suggest that the highest values of  $\Delta^{14}\text{C}_{\text{atm}}$  occurred during the Laschamp excursion, with  
522 a maximum value of  $\sim 595$  permil at 41.1 kyr BP found in the IntCal13 record. The Hulu Cave record indicates even  
523 higher values for the Laschamp event  $\Delta^{14}\text{C}_{\text{atm}} = \sim 742$  permil, at 39.7 kyr BP). In contrast, the model is able to simulate  
524 maximum  $\Delta^{14}\text{C}_{\text{atm}}$  values of only  $\sim 364$  permil at 40.4 kyr BP, and  $\sim 236$  permil at 40.5 kyr BP, as predicted by the  
525 paleointensity-based and ice-core  $^{10}\text{Be}$ -based production rate estimates, respectively. Although the model is unable to  
526 reproduce the reconstructed values of  $\Delta^{14}\text{C}_{\text{atm}}$ , the modelled amplitude of the variation in  $\Delta^{14}\text{C}_{\text{atm}}$  in response to the  
527 Laschamp event shows a reasonable agreement with the reconstructed amplitude of  $\Delta^{14}\text{C}_{\text{atm}}$  change found in the  
528 IntCal13 record ( $\sim 240$  permil). The  $\Delta^{14}\text{C}_{\text{atm}}$  change predicted by paleointensity data has a maximal amplitude of about  
529 320 permil, whereas the ice-core  $^{10}\text{Be}$  data indicate a smaller amplitude ( $\sim 224$  permil). Note that the IntCal13 and  
530 model-simulated amplitudes of the Laschamp-related  $\Delta^{14}\text{C}_{\text{atm}}$  change are about two times smaller than that observed  
531 in the Hulu Cave record ( $\sim 575$  permil), which is more likely to be correct.

532

533 Moving onto the full glacial record (50 to 18 kyr BP), there are considerable discrepancies between  
534 reconstructed and modelled  $\Delta^{14}\text{C}_{\text{atm}}$  ( $\Delta\Delta^{14}\text{C}$ ; see Fig. 7). The use of ice-core  $^{10}\text{Be}$  data to predict past changes in  $\Delta^{14}\text{C}_{\text{atm}}$   
535 results in the largest  $\Delta\Delta^{14}\text{C}$ , with offsets between the records as high as  $\sim 544$  to 558 permil (root-mean-square error  
536  $RMSE = 404$  to 408 permil). Model-simulated  $\Delta^{14}\text{C}_{\text{atm}}$  given by paleointensity data varies widely between the four  
537 available reconstructions, yielding  $\Delta\Delta^{14}\text{C}$  values of  $\sim 325$  to 639 permil ( $RMSE = 206$  to 455 permil). Note that the  
538 upper limit of the paleointensity-based  $\Delta\Delta^{14}\text{C}$  overlaps with the ice-core  $^{10}\text{Be}$ -based  $\Delta\Delta^{14}\text{C}$ . Given the uncertainties  
539 associated with the reconstruction of past changes in  $^{14}\text{C}$  production, accurate predictions of its contribution to past  
540 changes in  $\Delta^{14}\text{C}_{\text{atm}}$  are challenging. Nonetheless, the substantial systematic offsets between the reconstructed and  
541 model-simulated  $\Delta^{14}\text{C}_{\text{atm}}$  records after  $\sim 33$  kyr BP point toward insufficiently high  $^{14}\text{C}$  production rates over this period  
542 of time. The question arises as to whether another factor besides geomagnetic modulation of the cosmic ray intensity  
543 was responsible for elevated glacial  $\Delta^{14}\text{C}_{\text{atm}}$  levels. The effect of ocean carbon cycle changes on the evolution of  
544  $\Delta^{14}\text{C}_{\text{atm}}$  is considered next.

545

### 546 3.3 Carbon cycle contribution to high glacial atmospheric $\Delta^{14}\text{C}$ levels

547

548 Here we investigate the magnitude and timing of the maximum possible  $\Delta^{14}\text{C}_{\text{atm}}$  change during the last glacial period,  
549 obtained by running the Bern3D model with eight different carbon cycle scenarios (see Table 1). For the sake of

550 clarity, we will discuss only the results of model runs using the mean paleointensity-based  $^{14}\text{C}$  production rate, though  
551 all available reconstructions were used. We emphasize that this is not a best-guess estimate of paleointensity-based  
552  $^{14}\text{C}$  production. One should focus on the relative changes of  $\Delta^{14}\text{C}_{\text{atm}}$  between model scenarios, and how specific carbon  
553 cycle processes affect the glacial level of  $\Delta^{14}\text{C}_{\text{atm}}$ .

554  
555 Modelled 50,000-year records of  $\Delta^{14}\text{C}_{\text{atm}}$  and  $\text{CO}_2$  as well as their reconstructed histories are shown in Fig.  
556 8. In order to provide a basis for comparison of modelling efforts, the results of model run MOD (which assumes a  
557 constant preindustrial carbon cycle) are presented. The influence of ocean carbon cycle changes on  $\Delta^{14}\text{C}_{\text{atm}}$  was tested  
558 in the other model runs. Interestingly, the forcing fields for model run PAL (orbital parameters, greenhouse gas  
559 radiative forcing, and ice sheet extent) have only a minimal impact on  $\Delta^{14}\text{C}_{\text{atm}}$ . The PAL forcing fields also do not  
560 achieve sufficiently low glacial  $\text{CO}_2$  concentrations. Only a slight reduction of atmospheric  $\text{CO}_2$  by  $\sim 20$  ppm could be  
561 achieved, which unrealistically occurs during the last glacial termination ( $\text{CO}_2 = 258.07$  ppm, at 14.6 kyr BP). With  
562 hypothetical carbon cycle changes, the agreement between observed and modelled  $\text{CO}_2$  during the last glacial period  
563 is good (as by design), but the deglacial  $\text{CO}_2$  rise is lagged and  $\sim 60$  ppm too small at 11 kyr BP. Since this study  
564 focuses on glacial  $\Delta^{14}\text{C}_{\text{atm}}$  levels before incipient deglaciation at  $\sim 18$  kyr BP, we will not discuss the lag any further.

565  
566 Model simulation of high glacial  $\Delta^{14}\text{C}_{\text{atm}}$  levels can be significantly improved by considering hypothetical  
567 carbon cycle changes in conjunction with PAL forcing. The amplitude of  $\Delta^{14}\text{C}_{\text{atm}}$  change is highest for runs CIRC,  
568 VENT, and VENTx. This behavior is due to the fact that, owing to a reduction of  $\tau$ ,  $K_V$ , and  $k_w$ , strong vertical  $\Delta^{14}\text{C}$   
569 gradients in the ocean, as well as a large air-sea  $\Delta^{14}\text{C}$  gradient, are established. As shown in Fig. 8, a more sluggish  
570 ventilation of deep waters is clearly expressed as an increase in the model ocean's global average ideal age and surface-  
571 and deep-water reservoir ages, where the latter two are calculated for the surface ocean and bottom water grid cells,  
572 respectively. These are equivalent to radiocarbon reservoir age offsets following Soulet et al. (2016). The deep-water  
573 reservoir age (i.e., B-Atm  $^{14}\text{C}$  age offset, or B-Atm) provides a measure of the radiocarbon disequilibrium between  
574 the deep ocean and the atmosphere, which arises due to the combined effect of air-sea gas exchange efficiency and  
575 the deep ocean ventilation rate, whereas the effect of upper ocean stratification and/or sea ice on air-sea gas exchange  
576 is particularly important for surface reservoir ages (i.e., surface R-age) (Skinner et al., 2019).

577  
578 Driven by a reduction in ocean circulation, model run CIRC predicts a substantial increase in B-Atm during  
579 the last glacial, which is defined here as 40 to 18 kyr BP to avoid biasing global mean estimates toward Laschamp  
580 values. The global average glacial B-Atm predicted by CIRC is  $\sim 3225$   $^{14}\text{C}$  years, representing an increase in B-Atm  
581 of  $\sim 1599$   $^{14}\text{C}$  years relative to the preindustrial value of  $\sim 1626$   $^{14}\text{C}$  years. Model run VENT predicts a slightly larger  
582 increase in glacial B-Atm due to the inhibition of air-sea gas exchange. The “oldest” glacial waters are found in model  
583 run VENTx where air-sea gas exchange is severely restricted, yielding an increase in B-Atm of  $\sim 1912$   $^{14}\text{C}$  years  
584 (glacial B-Atm  $\sim 3538$   $^{14}\text{C}$  years). The glacial B-Atm values given by runs CIRC, VENT, and VENTx, as well as the  
585  $\sim 717$  year increase in ideal age during the last glacial relative to preindustrial, suggest that the glacial deep ocean was  
586 about two times older than its preindustrial counterpart. Comparison of our LGM B-Atm estimates (range of 3682 to



587 3962  $^{14}\text{C}$  years) with the compiled LGM marine radiocarbon data of Skinner et al. (2017) demonstrate that the carbon  
588 cycle scenarios are extreme, although it should be noted that Skinner et al. consider a wider depth range (~500 to 5000  
589 m) of the ocean than we do. Skinner et al. (2017) predict a global average LGM B-Atm value of ~2048  $^{14}\text{C}$  years, an  
590 increase of ~689  $^{14}\text{C}$  years relative to preindustrial. Turning our comparison to surface reservoir ages, we note that  
591 our global average LGM surface R-age of ~1132  $^{14}\text{C}$  years from runs VENT and VENTx is comparable to the ~1241  
592  $^{14}\text{C}$  years obtained by Skinner et al. (2017) for the LGM. The model-based estimates of surface R-age from Butzin et  
593 al. (2017) indicate a much lower LGM value of ~780  $^{14}\text{C}$  years, and values ranging from 540 to 1250  $^{14}\text{C}$  years between  
594 50 and 25 kyr BP. Note that these estimates are based on model-simulated values between 50°N and 50°S. If the polar  
595 regions are included in the calculation (see Fig. 8c), their surface R-age estimates become comparable to our glacial  
596 values (range of 911 to 1354  $^{14}\text{C}$  years), and between about 34 and 22 kyr BP can exceed them, including even those  
597 from model runs VENT and VENTx, unless  $\Delta^{14}\text{C}_{\text{atm}}$  and  $\text{CO}_2$  are prescribed (dashed colored lines in Fig. 8c) as in the  
598 simulation by Butzin et al. (2017).

599  
600 Indirect evidence for deep water ageing can be provided by the occurrence of depleted ocean interior oxygen  
601 levels, due to the progressive consumption of dissolved oxygen during organic matter remineralization in the water  
602 column. This situation is amplified by the slow escape of accumulating remineralized carbon in the ocean interior  
603 (see, e.g., Skinner et al., 2017), leading to higher values of apparent oxygen utilization ( $\text{AOU} = \text{O}_{2,\text{pre}} - \text{O}_2$ ). These  
604 two concepts (increased AOU and increased B-Atm) taken together signal a significant reduction in deep ocean  
605 ventilation characterized by a decrease in the exchange rate between younger (higher  $\Delta^{14}\text{C}$ ) surface waters and older  
606 ( $^{14}\text{C}$ -depleted), carbon-rich deep waters. Model runs CIRC, VENT, and VENTx do indeed indicate a large increase in  
607 AOU of about 95  $\text{mmol m}^{-3}$  from its preindustrial value of ~150  $\text{mmol m}^{-3}$ . The reason for this AOU increase is that  
608 a reduction of deep ocean ventilation permits enhanced accumulation of remineralized carbon in the ocean interior  
609 and therefore a more efficient biological carbon pump. Model runs BIO, PHYS-BIO, and PHYS-BIOx allow us to  
610 investigate the impact of other biological carbon pump changes on  $\Delta^{14}\text{C}_{\text{atm}}$  and  $\text{CO}_2$  (i.e., changes in the  $\text{CaCO}_3$ -to-  
611 POC export ratio and POC remineralization length scale). While these changes lead to an effective atmospheric  $\text{CO}_2$   
612 drawdown mechanism, model results confirm that their effect on  $\Delta^{14}\text{C}_{\text{atm}}$  is much less important (see Fig. 8).

613  
614 Model run VENTx gives the best results with respect to glacial levels of  $\Delta^{14}\text{C}_{\text{atm}}$ , with a maximum  
615 underestimation of ~202 to 229 permil ( $\text{RMSE} = 103$  to 110 permil) and a relatively good correlation ( $r = 0.79$  to  
616 0.91). Only one model parameter was changed for run VENTx as compared to runs CIRC and VENT, namely, the  
617 polar gas transfer velocity  $k_w$  was reduced to 0 percent of its preindustrial value during the last glacial. In this extreme  
618 scenario, we assume that sea ice cover extended in the northern hemisphere as far south as 60°N and in the southern  
619 hemisphere as far north as 48°S, which is not supported by the reconstructions (Gersonde et al., 2005; Allen et al.,  
620 2011). Nonetheless, considering extreme assumptions about polar air-sea exchange efficiency under glacial climate  
621 conditions is interesting for two reasons: (1) a change in gas exchange hardly affects the atmospheric  $\text{CO}_2$   
622 concentration, and (2) an additional change of  $\Delta^{14}\text{C}_{\text{atm}}$  could possibly be achieved on a time scale of tens of thousands  
623 of years by changing the balance between weathering and sedimentation (see Sect. 3.1.3). This behavior has important

624 implications for the glacial atmosphere, which is characterized by high  $\Delta^{14}\text{C}$  levels in conjunction with low but  
625 relatively stable  $\text{CO}_2$  concentrations. In contrast to a change in ocean circulation, air-sea gas exchange is a dedicated  
626  $\Delta^{14}\text{C}_{\text{atm}}$  “control knob” that can be invoked by models for a further increase of  $\Delta^{14}\text{C}_{\text{atm}}$  without changing atmospheric  
627  $\text{CO}_2$ . Here, an additional increase in  $\Delta^{14}\text{C}_{\text{atm}}$  of  $\sim 130$  permil relative to CIRC and VENT is achieved if gas exchange  
628 is reduced permanently to 0 percent in the polar regions.

629  
630 While the modelled  $\Delta^{14}\text{C}_{\text{atm}}$  values obtained by VENTx show rather good agreement with the reconstructions  
631 between 50 and 33 kyr BP ( $r = 0.92$  to  $0.96$ ;  $RMSE = 74$  to  $102$  permil), considerable discrepancies remain for the  
632 younger portion of the record. The analysis shown in Fig. 9 illustrates that even with extreme changes in the ocean  
633 carbon cycle it is very difficult to reproduce the reconstructed  $\Delta^{14}\text{C}_{\text{atm}}$  values after  $\sim 33$  kyr BP. During this period of  
634 time, VENTx underestimates  $\Delta^{14}\text{C}_{\text{atm}}$  by up to  $\sim 203$  permil ( $RMSE = 118$  to  $128$  permil), and is very poorly ( $r = 0.1$ )  
635 correlated with the reconstructions, confirming that there are still considerable gaps in our understanding. Although it  
636 may be possible that permanent North Atlantic-Arctic and Antarctic sea ice cover extended to lower and higher  
637 latitudes than previously reconstructed, we conclude from our model study that even extreme assumptions about sea  
638 ice cover are insufficient to explain the elevated  $\Delta^{14}\text{C}_{\text{atm}}$  levels after  $\sim 33$  kyr BP. It appears instead that the glacial  $^{14}\text{C}$   
639 production rate was higher than previously estimated and/or the reconstruction of glacial  $\Delta^{14}\text{C}_{\text{atm}}$  levels is biased high.  
640 The older portion of the  $\Delta^{14}\text{C}_{\text{atm}}$  record is based on data from archives other than tree rings (i.e., plant macrofossils,  
641 speleothems, corals, and foraminifera) (Reimer et al., 2013), providing, except for the Lake Suigetsu plant macrofossil  
642 data (Bronk Ramsey et al., 2012), only indirect measurements of  $\Delta^{14}\text{C}_{\text{atm}}$ . Note that these data show uncertainty in  
643 calendar age that propagate into the estimation of past  $\Delta^{14}\text{C}_{\text{atm}}$  levels.

644  
645 Large uncertainties in the pre-Holocene  $^{14}\text{C}$  production rate also hamper our qualitative and quantitative  
646 interpretation of the  $\Delta^{14}\text{C}_{\text{atm}}$  record. There is considerable disagreement between the available reconstructions of past  
647 changes in  $^{14}\text{C}$  production (Fig. 1). Paleointensity-based estimates typically predict higher  $^{14}\text{C}$  production rates than  
648 ice-core  $^{10}\text{Be}$ -based ones. An exception is the paleointensity stack from Channell et al. (2018), which predicts lower  
649 production rates. But, irrespective of the scatter, it is clear that all of the  $^{14}\text{C}$  production rate estimates are insufficiently  
650 high to explain the elevated  $\Delta^{14}\text{C}_{\text{atm}}$  levels during the last glacial. Given the uncertainties in these estimates, it is very  
651 difficult to quantitatively describe the role of the ocean carbon cycle in determining the  $\Delta^{14}\text{C}$  and  $\text{CO}_2$  levels in the  
652 glacial atmosphere.

### 654 3.4 Reconstructing the $^{14}\text{C}$ production rate by deconvolving the atmospheric $\Delta^{14}\text{C}$ record

655  
656 The unresolved discrepancy between reconstructed and model-simulated  $\Delta^{14}\text{C}_{\text{atm}}$  raises the question how the  $^{14}\text{C}$   
657 production rate would have had to evolve to be consistent with the IntCal13 calibration curve or the new Hulu Cave  
658  $\Delta^{14}\text{C}_{\text{atm}}$  dataset. This question is addressed by deconvolving the  $\Delta^{14}\text{C}_{\text{atm}}$  reconstruction over the last 50 kyr, using the  
659 Bern3D carbon cycle model forced with reconstructed histories of  $\Delta^{14}\text{C}_{\text{atm}}$  and  $\text{CO}_2$  (see Eq. [2]). The carbon cycle  
660 scenarios described in Table 1, with the exception of MOD, are used in order to provide an estimate of the uncertainty

661 associated with the model's glacial ocean carbon cycle. We note that the carbon cycle scenarios are not designed to  
662 capture the specific features of the last glacial termination, and therefore the results of the deconvolution over this  
663 time period must be considered very preliminary (and regarded as tentative). A detailed analysis of the Holocene  $^{14}\text{C}$   
664 production rate is available in the literature (Roth and Joos, 2013). Finally, we consider the uncertainties associated  
665 with the older portion of the  $\Delta^{14}\text{C}_{\text{atm}}$  record by deconvolving both the IntCal13 and Hulu Cave  $\Delta^{14}\text{C}_{\text{atm}}$  records. Hulu  
666 Cave data overlap with IntCal13 between  $\sim 10.6$  and  $33.3$  kyr BP (Cheng et al., 2018), as expected from the fact that  
667 IntCal13 between  $10.6$  and  $26.8$  kyr BP is based in part on Hulu Cave stalagmite H82 (Southon et al., 2012), whereas  
668 there are substantial offsets before  $\sim 30$  kyr BP.

669  
670 Fig. 10 shows the new, model-based reconstruction of past changes in  $^{14}\text{C}$  production compared with  
671 available measurement-based reconstructions. Before the onset of the Laschamp excursion at  $\sim 42$  kyr BP, production  
672 rates as inferred from the Hulu Cave record are near modern levels, whereas those obtained from the IntCal13 record  
673 are somewhat higher than modern. As expected, peak production occurs during the Laschamp event ( $\sim 42$  to  $40$  kyr  
674 BP), with the Hulu Cave dataset yielding the largest amplitude (factor of  $\sim 2$  greater than modern). The IntCal13 record  
675 predicts a smaller amplitude of  $\sim 1.6$  times the modern value. Both  $\Delta^{14}\text{C}_{\text{atm}}$  records predict production minima at  $\sim 37$   
676 kyr BP ( $\sim 7$  percent higher than modern) and  $\sim 32$  kyr BP ( $\sim 5$  percent higher than modern), interrupted by a prominent  
677 peak (factors of  $\sim 1.5$  and  $\sim 1.4$ , respectively) during the Mono Lake geomagnetic excursion ( $\sim 34$  kyr BP), though the  
678 details of the timing and structure differ between the two records. Between  $32$  and  $22$  kyr BP, model-based estimates  
679 of the  $^{14}\text{C}$  production rate are  $\sim 1.3$  times the modern value, which then decrease to around modern levels by HS1 ( $\sim 18$   
680 kyr BP).

681  
682 Model-based estimates of  $^{14}\text{C}$  production during the last glacial are typically higher than paleointensity-based  
683 and ice-core  $^{10}\text{Be}$ -based ones, as expected from Sect. 3.2. Between  $32$  and  $22$  kyr BP, the deconvolutions of the  
684 IntCal13 and Hulu Cave  $\Delta^{14}\text{C}_{\text{atm}}$  records give estimates that are about  $17.5$  percent higher than the reconstructions. It  
685 is important to note that the differences between the reconstructions based on proxy data (i.e., paleointensity data and  
686 ice-core  $^{10}\text{Be}$  fluxes) are as large as the differences between our deconvolution results and the reconstructions (see  
687 Table 2). As shown in Fig. 11, it is extremely difficult to reconcile the discrepancies between measurement- and  
688 model-based  $^{14}\text{C}$  production on the basis of carbon cycle changes alone. Nonetheless, the fact remains that two  
689 independent estimates of the  $^{14}\text{C}$  production rate (i.e., estimates inferred from paleointensity data and from ice-core  
690  $^{10}\text{Be}$  fluxes) show systematically lower rates than those obtained by our model-based deconvolution of  $\Delta^{14}\text{C}_{\text{atm}}$ , in  
691 particular between  $32$  and  $22$  kyr BP. The differences between the production rate results shown in Fig. 10 and Fig.  
692 11 and Table 2 stem from various uncertainties that are discussed next.

693  
694 Uncertainties associated with the glacial ocean carbon cycle (Fig. 10, colored shading; Fig. 11, colored lines)  
695 are systematic in our approach. The deconvolutions, e.g., of the Hulu Cave  $\Delta^{14}\text{C}_{\text{atm}}$  record, under different model  
696 scenarios are offset against one another, whereas the millennial-scale variability is maintained (see Fig. 11). We do  
697 not attempt to resolve uncertainties associated with Dansgaard-Oeschger warming events and related Antarctic and

698 tropical climatic excursions in the model runs. Such climatic events may have influenced the atmospheric radiocarbon  
699 budget, but their influence on long-term variations in  $\Delta^{14}\text{C}_{\text{atm}}$ , and therefore inferred production rates, is presumably  
700 limited. As may be expected, the lowest production rates (the lowest  $F_{\text{as}}$  values) are found in VENTx and the highest  
701 in scenarios PAL and BIO, mirroring the high and low glacial  $\Delta^{14}\text{C}_{\text{atm}}$  levels achieved by these model scenarios as  
702 discussed in Sect. 3.3. Note that there is a large uncertainty in the model-based  $^{14}\text{C}$  production rate stemming from  
703 uncertainties associated with the reconstruction of past changes in  $\Delta^{14}\text{C}_{\text{atm}}$ , in particular the older portion of the  $\Delta^{14}\text{C}_{\text{atm}}$   
704 record.

705  
706 A shortcoming of paleointensity-based reconstructions of the  $^{14}\text{C}$  production rate is that they neglect changes  
707 in the solar modulation of the cosmic radiation. The solar modulation potential, which describes the impact of the  
708 solar magnetic field on isotope production, varied between 100 and 1200 MeV during the Holocene on decadal to  
709 centennial time scales, with a median value of approximately 565 MeV (Roth and Joos, 2013). A halving of the solar  
710 modulation potential (e.g., from 600 to 300 MeV) increases the  $^{14}\text{C}$  production rate by about 25 percent for the modern  
711 geomagnetic field strength (Roth and Joos, 2013; see their Fig. 13). This sensitivity remains similar when changes in  
712 the strength of the geomagnetic field are limited as during the last  $\sim 35$  kyr (Muscheler and Heikkilä, 2011). A shift to  
713 lower solar modulation potential could have materialized if the sun spent on average more time in the postulated  
714 “Grand Minimum” mode (Usoskin et al., 2014) during the last glacial than during the Holocene. The sensitivity of  
715 isotope production to variations in solar modulation potential becomes large during the Laschamp event when the  
716 intensity of the geomagnetic field was close to zero and changes in the solar modulation of the cosmic ray flux may  
717 have a discernible impact on the high  $\Delta^{14}\text{C}_{\text{atm}}$  levels found over this period. A reduction of the solar modulation  
718 potential from 600 to 0 MeV would double  $^{14}\text{C}$  production during times of zero geomagnetic field strength (Masarik  
719 and Beer, 2009). However, it is likely that changes in the solar modulation potential were insufficient to explain the  
720 discrepancy between paleointensity-based production rate estimates and the results of our deconvolution, in particular  
721 for the post-Laschamp period and for the reconstruction by Channell et al. (2018). Uncertainties associated with the  
722 paleointensity-based reconstructions stem also from uncertainties in estimating the age-scales of the marine sediments  
723 and the geomagnetic field data.

724  
725 The ice-core  $^{10}\text{Be}$ -based reconstruction of past changes in  $^{14}\text{C}$  production reflects, by definition, the combined  
726 influence of changes in the solar and geomagnetic modulation of the cosmic ray flux reaching the Earth. This method,  
727 therefore, avoids a fundamental shortcoming of reconstructions based on geomagnetic field data. The assumption is  
728 that the  $^{10}\text{Be}$  and  $^{36}\text{Cl}$  deposited on polar ice and measured in ice cores scales with the amount of cosmogenic isotopes  
729 in the atmosphere. A difficulty is to extrapolate measurements from a single or a few locations to the global  
730 atmosphere. Changes in climate influence atmospheric transport and deposition of  $^{10}\text{Be}$  as well as the snow  
731 accumulation rate, which affect the ice-core  $^{10}\text{Be}$  concentration (Elsässer et al., 2015). Furthermore, the sensitivity of  
732  $^{10}\text{Be}$  in polar ice versus the sensitivity of total production to magnetic field variations, or “polar bias”, is a point of  
733 debate, but atmospheric transport models (Heikkilä et al., 2009; Field et al., 2006) and data analyses (Bard et al.,  
734 1997; Adolphi and Muscheler, 2016; Adolphi et al., 2018) reach different conclusions about its existence and

735 magnitude. If a polar bias was present, it would lead to an underestimation of the geomagnetic modulation of the ice-  
736 core  $^{10}\text{Be}$  flux, and therefore variations in the  $^{10}\text{Be}$ -based  $^{14}\text{C}$  production rate would also be underestimated. However,  
737 the mismatch of up to  $\sim 544$  to  $558$  permil between reconstructed and modelled  $^{10}\text{Be}$ -based  $\Delta^{14}\text{C}_{\text{atm}}$  during the last  
738 glacial (see Fig. 7c) appears to be much too large to be reconciled by considering uncertainties in the polar bias alone.  
739 Furthermore, this mismatch with reconstructed  $\Delta^{14}\text{C}_{\text{atm}}$  is qualitatively similar when using paleointensity-based  $^{14}\text{C}$   
740 production rates that do not suffer from a polar bias (Fig. 7c).

741  
742 Given the uncertainties associated with the proxy records, it may not be surprising that estimates of the  $^{14}\text{C}$   
743 production rate for the last 50 kyr, as obtained by three fundamentally different methods (geomagnetic field data from  
744 marine sediments,  $^{10}\text{Be}$  and  $^{36}\text{Cl}$  measurements in polar ice cores, and model-based deconvolution of  $\Delta^{14}\text{C}_{\text{atm}}$ ), disagree  
745 with one another, typically by order 10 percent and sometimes by up to 100 percent. At the same time, it is intriguing  
746 that two independent estimates of the  $^{14}\text{C}$  production rate (i.e., estimates inferred from paleointensity and ice-core  $^{10}\text{Be}$   
747 data) give values that are systematically lower than what is required to match the  $\Delta^{14}\text{C}_{\text{atm}}$  reconstruction.

#### 748 749 **4 Summary and conclusions**

750  
751 It is generally assumed that  $\Delta^{14}\text{C}_{\text{atm}}$  is controlled by abiotic processes such as atmospheric  $^{14}\text{C}$  production, air-sea gas  
752 exchange, and ocean circulation and mixing. Here, results from sensitivity experiments with the Bern3D earth system  
753 model of intermediate complexity suggest that  $\Delta^{14}\text{C}_{\text{atm}}$  is potentially quite sensitive to the interaction with the ocean  
754 sediments on multimillennial time scales. This rather surprising result is due to the coupling of ocean circulation and  
755 the sedimentation of biogenic material on the sea floor via the biological carbon pump, which has important  
756 implications for the ocean carbon inventory. If the model's ocean carbon cycle is sufficiently perturbed, e.g., by  
757 changing the inputs or parameters controlling ocean circulation and/or gas exchange, the imbalance between  
758 weathering and sedimentation has a significant impact on the total oceanic amount of carbon. On time scales of tens  
759 of thousands of years this slow change in the ocean carbon inventory influences the partitioning of  $^{14}\text{C}/\text{C}$  between the  
760 ocean and atmosphere, and thus also oceanic  $\Delta^{14}\text{C}$  and  $\Delta^{14}\text{C}_{\text{atm}}$ . This is important information for long-term climate  
761 studies and paleoclimate modelling efforts concerning  $\Delta^{14}\text{C}_{\text{atm}}$ . Note that the representation of terrestrial weathering  
762 and sea floor sedimentation in the Bern3D is necessarily simplified compared to reality. Nonetheless, a change in the  
763 ocean carbon inventory linked with the weathering/sedimentation balance should be discussed as one of the potentially  
764 important factors affecting  $\Delta^{14}\text{C}_{\text{atm}}$  during the last glacial period.

765  
766 The reason for the high  $\Delta^{14}\text{C}$  values exhibited by the glacial atmosphere is still not clear. In order to  
767 investigate potential mechanisms governing glacial  $\Delta^{14}\text{C}_{\text{atm}}$  levels, the Bern3D model is again used as a tool. Results  
768 of model simulations forced only by production changes point out that none of the available reconstructions of the  $^{14}\text{C}$   
769 production rate can explain the full amplitude of  $\Delta^{14}\text{C}_{\text{atm}}$  change during the last glacial. In order to test the sensitivity  
770 of the model results with respect to the ocean carbon cycle state, various model parameters, i.e., different sets of  
771 physical and biogeochemical parameters, were “tuned” to match the glacial  $\text{CO}_2$  level. From this, we find that  $\Delta^{14}\text{C}_{\text{atm}}$

772 is most sensitive to changes in physical model parameters, in particular those controlling ocean circulation and gas  
773 exchange. In order to achieve an  $\Delta^{14}\text{C}_{\text{atm}}$  value close to the glacial level, the gas transfer velocity in the polar regions  
774 had to be reduced by 100 percent. If interpreted as being due to a greater extent of permanent sea ice cover, a reduction  
775 in polar air-sea exchange efficiency is a possible explanation for high glacial  $\Delta^{14}\text{C}_{\text{atm}}$  levels. Although this hypothesis  
776 is compelling, such a scenario is not supported by the proxy records of Antarctic sea ice cover (Gersonde et al., 2005;  
777 Allen et al., 2011) and the  $^{13}\text{C}/^{12}\text{C}$  ratio of atmospheric  $\text{CO}_2$  (Eggleston et al., 2016).

778  
779 Atmospheric  $\Delta^{14}\text{C}$  that is modelled at any point in time reflects  $^{14}\text{C}$  production at that point, as well as the  
780 legacy of past production and carbon cycle changes. The question arises as to whether our conclusions are affected by  
781 unaccounted legacy effects, e.g., linked to the preindustrial spin-up simulation or model-diagnosed production rates.  
782 Transient simulations forced by reconstructed changes in  $^{14}\text{C}$  production (Sect. 3.2 and 3.3) are initialized at 70 kyr  
783 BP, but their interpretation is restricted to the last 50,000 years of the integration to minimize legacy effects from  
784 model spin-up. Available reconstructions of the  $^{14}\text{C}$  production rate in relative units (Sect. 2.5) are applied as a scale  
785 factor to the preindustrial steady-state absolute value, which is diagnosed by running the Bern3D model to equilibrium  
786 under preindustrial boundary conditions. This approach represents an approximation and equilibrium conditions do  
787 not fully apply. Indeed, there is a mismatch between reconstructed and modelled  $\Delta^{14}\text{C}_{\text{atm}}$  at the preindustrial (see Fig.  
788 8a). This mismatch is on the order of a few percent or less and adjusting the base level of production accordingly  
789 would not remove the large mismatch between reconstructed and modelled  $\Delta^{14}\text{C}_{\text{atm}}$  during the last glacial. In addition,  
790 the uncertainty in the absolute value of the preindustrial production rate is on the order of 15%, primarily due to the  
791 uncertainties in the preindustrial ocean radiocarbon inventory (see Roth and Joos, 2013, Sect. 3.2). This potential  
792 systematic bias, however, does not affect our conclusions as we consider normalized production rate changes (see Fig.  
793 7, 10, and 11).

794  
795 Before model-simulated  $\Delta^{14}\text{C}_{\text{atm}}$  can be taken seriously, it must be demonstrated that the reconstruction of  
796 past changes in  $^{14}\text{C}$  production is reliable. There is, however, a substantial amount of scatter in the paleointensity-  
797 based and ice-core  $^{10}\text{Be}$ -based estimates of  $^{14}\text{C}$  production. Here we adopt an alternative approach to estimating the  
798  $^{14}\text{C}$  production rate, which would indeed benefit from further constraints and lines of supporting evidence. Our  
799 deconvolution-based approach assumes that the  $^{14}\text{C}$  production rate can be derived from an atmospheric radiocarbon  
800 budget, constructed using a prognostic carbon cycle model combined with the  $\Delta^{14}\text{C}_{\text{atm}}$  record. Here, non-equilibrium  
801 effects are fully accounted for by transient simulations where  $\Delta^{14}\text{C}_{\text{atm}}$  and  $\text{CO}_2$  are prescribed following their  
802 reconstructed histories (Sect. 3.4). Yet, these simulations indicate that the discrepancy between measurement- and  
803 model-based estimates of the  $^{14}\text{C}$  production rate remains for the last glacial (Fig. 10b). This would suggest that  
804 unaccounted legacy effects do not significantly affect our conclusions. Our model results imply that the glacial  $^{14}\text{C}$   
805 production rate as inferred from paleointensity data and ice-core  $^{10}\text{Be}$  fluxes may be underestimated by about 15  
806 percent between 32 and 22 kyr BP, a time interval which appears to be an important piece of the glacial-interglacial  
807  $\Delta^{14}\text{C}_{\text{atm}}$  puzzle. Note that our model-based estimates are associated with uncertainties arising from the reconstruction  
808 of the older portion of the  $\Delta^{14}\text{C}_{\text{atm}}$  record and from the model simulation of the glacial ocean carbon cycle (e.g.,

809 uncertainties in the glacial ocean circulation and air-sea CO<sub>2</sub> fluxes). An improved understanding of the role of <sup>14</sup>C  
810 production in past changes of  $\Delta^{14}\text{C}_{\text{atm}}$  would open up the possibility of attributing model deficiencies to real changes  
811 in the ocean carbon cycle, but there is as yet no emerging single record of the <sup>14</sup>C production rate.

812  
813 Progress in several different areas may help to resolve the glacial-interglacial radiocarbon problem.  
814 Additional records of glacial  $\Delta^{14}\text{C}_{\text{atm}}$  would help refine the older portion of the IntCal  $\Delta^{14}\text{C}$  record. Cosmogenic isotope  
815 production records may be improved, e.g., by refining estimates of ice accumulation, by developing a better  
816 understanding of <sup>10</sup>Be transport and deposition during the glacial, by recovering additional long and continuous  
817 records from Antarctic ice cores and including marine <sup>10</sup>Be records, and by obtaining additional geomagnetic field  
818 data. An expanded spatiotemporal observational coverage of  $\Delta^{14}\text{C}$  of DIC in the surface and deep ocean would help  
819 narrow the time scales of surface-to-deep transport and air-sea equilibration of  $\Delta^{14}\text{C}$ , carbon and nutrients, and thereby  
820 guide model-based analyses. Models should become more sophisticated and detailed in order to reproduce  
821 successfully the glacial-interglacial changes in carbon and radiocarbon, by including exchange with sediments and the  
822 lithosphere and by better representing coastal processes, and by representing a wide variety of paleo proxies such as  
823  $\delta^{13}\text{C}$ , Nd isotopes, carbonate ion concentration, lysocline evolution, and paleo-productivity proxies in a 3-D dynamic  
824 context for model evaluation. What is also missing are methods to quantify how the ocean carbon inventory, which  
825 co-determines the <sup>14</sup>C/C ratio and thus the  $\Delta^{14}\text{C}$  values in the ocean and atmosphere, has changed over the last 50,000  
826 years. Ultimately, an improved knowledge of <sup>14</sup>C production during the last glacial, as well as more robust constraints  
827 on the prevailing climate conditions (e.g., ocean circulation, sea ice cover, and wind speed), are necessary to elucidate  
828 the processes permitting mysteriously high  $\Delta^{14}\text{C}$  levels in the glacial atmosphere.

## 829 830 **Appendix A: Description of the Bern3D model**

831  
832 The physical core of the Bern3D model is based on the 3-D rigid-lid ocean model of Edwards et al. (1998) as updated  
833 by Edwards and Marsh (2005). The forcing fields for the model integration are monthly mean wind stress data taken  
834 from NCEP/NCAR (Kalnay et al., 1996). Diapycnal mixing is parameterized with a uniform vertical diffusivity  $K_V$  of  
835  $2 \times 10^{-5} \text{ m s}^{-1}$ . The parameterization of eddy-induced transport is separated from that of isopycnal mixing, using the  
836 Gent-McWilliams skew flux (Griffies, 1998). Running at the same temporal and horizontal resolution, the one-layer  
837 energy-moisture balance atmosphere model performs an analysis of the energy budget of the Earth by involving solar  
838 radiation, infrared fluxes, evaporation and precipitation, and sensible and latent heat. The zonally averaged surface  
839 albedo climatology is taken from Kukla and Robinson (1980). Transport of moisture is performed by diffusion and  
840 advection and heat by eddy diffusion.

841  
842 The Bern3D ocean carbon cycle model is based on the Ocean Carbon-Cycle Model Intercomparison Project  
843 (OCMIP-2) protocols. Air-sea gas exchange is parameterized using the standard gas transfer formulation adopted for  
844 OCMIP-2, except that the gas transfer velocity  $k_w$  parameterization is a linear function of wind speed (Krakauer et  
845 al., 2006) to which we have added a scale factor of 0.81 to match the observed global ocean inventory of bomb <sup>14</sup>C

846 (Müller et al., 2008). It is assumed that CO<sub>2</sub> and O<sub>2</sub> are well-mixed in the atmosphere. Surface boundary conditions  
847 also include a virtual-flux term for biogeochemical tracers (e.g., DIC and Alk) to account for their dilution or  
848 concentration due to implicit freshwater fluxes. Following OCMIP-2 biotic protocol, new production is partitioned  
849 into particulate and dissolved organic matter. Modifications from the original OCMIP-2 biotic protocol include the  
850 prognostic formulation of new/export production as a function of light, temperature, and limiting nutrient  
851 concentrations, where the nutrient uptake follows Michaelis-Menten kinetics. The production of biogenic CaCO<sub>3</sub> and  
852 opal is computed on the basis of the modelled particulate organic carbon (POC) production and availability of silicate,  
853 with a maximum possible fraction of CaCO<sub>3</sub> material that can be produced. This threshold value is represented by the  
854 CaCO<sub>3</sub>-to-POC export ratio. In the preindustrial control run, the global mean export ratio  $rr$  is 0.082.

855

856 Biogenic particles that have been produced in the 75-m production zone are redistributed over the water  
857 column in order to parameterize the downward particle flux through the water column. A power-law model referred  
858 to as the Martin curve is used to describe the vertical POC flux profile, whereas both CaCO<sub>3</sub> and opal export are  
859 redistributed over the water column with an exponential curve. POC is remineralized instantaneously back to dissolved  
860 form according to Redfield stoichiometry and with a 250-m length scale  $l_{POC}$  (i.e., in 250 m, the POC flux declines  
861 by  $1 - 1/e \approx 63$  percent). Likewise, CaCO<sub>3</sub> and opal are dissolved within one time step, with  $e$ -folding depths of  
862 5066 and 10,000 m, respectively. Biogenic particles reaching the model's sea floor form the upper boundary condition  
863 of the 10-layer sediment model after Heinze et al. (1999) and Gehlen et al. (2006). The sediment model includes four  
864 solid sediment components (POC, CaCO<sub>3</sub>, opal, and clay) and is based on the sediment advection and accumulation  
865 scheme as in the work of Archer et al. (1993). The rate of POC remineralization in the sediments is primarily  
866 determined by the pore water concentration of oxygen, whereas the mineral dissolution rate is governed by the  
867 saturation state of sediment pore waters with respect to CaCO<sub>3</sub> or opal. Weathering (dissolution) of carbonate and  
868 silicate rocks on land, phosphorous release by chemical weathering of rocks, and volcanic outgassing of CO<sub>2</sub> are  
869 simulated as constant inputs of DIC, Alk, phosphate (P), and silicate (Si) to the ocean at rates intended to balance their  
870 removal from the ocean by sedimentation on the sea floor. These weathering inputs are added as a constant increment  
871 to each surface ocean grid cell along the coastlines. The preindustrial steady state of the model is used to diagnose the  
872 weathering rates that are held fixed and constant throughout the simulations. Note that the preindustrial spin-up results  
873 in steady-state values for weathering-derived inputs of DIC, Alk, P, and Si of 0.46 Gt C per year, 34.37 Tmol Alk per  
874 year, 0.17 Tmol P per year, and 6.67 Tmol Si per year, respectively. These values are within the range of observational  
875 estimates (see, e.g., Jeltsch-Thömmes et al., 2019). Additional details concerning the sediment model are provided in  
876 Tschumi et al. (2011), while the appendix of Jeltsch-Thömmes et al. (2019) gives a detailed description of the  
877 atmosphere-ocean-sediment spin-up.

878

879 The exchange of any isotopic perturbation between the atmosphere and the terrestrial biosphere is simulated  
880 by use of the four-box model of Siegenthaler and Oeschger (1987). The terrestrial biosphere is represented by four  
881 well-mixed compartments (ground vegetation plus leaves, wood, detritus, and soils), with a fixed total carbon



882 inventory of 2220 Gt C. Net primary production is balanced by respiration of detritus and soils, and is set to 60 Gt C  
883 per year.

884

885 **Data availability.** Model-simulated atmospheric  $\Delta^{14}\text{C}$  presented in Fig. 7b and 8a, and model-based  $^{14}\text{C}$  production  
886 rates shown in Fig. 10a, are included in the Supplement. Other data generated or analyzed during this study can be  
887 made available upon request to the corresponding author (A.D.).

888

889 **Author contribution.** This study was designed by F.J. and A.D. with input from F.A. A.D. developed and  
890 performed the model simulations. F.A. provided production data. A.D. wrote the manuscript with contributions from  
891 the co-authors.

892

893 **Competing interests.** The authors declare that they have no conflict of interest.

894

895 **Acknowledgements.** This work was made possible by the Swiss National Science Foundation (#200020\_172476)  
896 and by the UniBE international 2021 fellowship program of the U. Bern. F.A. was supported by the Swedish  
897 Research Council (Vetenskapsrådet DNR: 2016-00218).

898

## 899 **References**

900

901 Adolphi, F., and Muscheler, R.: Synchronizing the Greenland ice core and radiocarbon timescales over the Holocene  
902 – Bayesian wiggle-matching of cosmogenic radionuclide records, *Climate of the Past*, 12, 15–30, 2016.

903 Adolphi, F., Muscheler, R., Svensson, A., Aldahan, A., Possnert, G., Beer, J., . . . Thiéblemont, R.: Persistent link  
904 between solar activity and Greenland climate during the Last Glacial Maximum, *Nature Geoscience*, 7,  
905 662–666, 2014.

906 Adolphi, F., Ramsey, C. B., Erhardt, T., Edwards, R. L., Cheng, H., Turney, C. S., . . . Muscheler, R.: Connecting  
907 the Greenland ice-core and U/Th timescales via cosmogenic radionuclides: testing the synchronicity of  
908 Dansgaard–Oeschger events, *Climate of the Past*, 14, 1755–1781, 2018.

909 Ahn, J., and Brook, E. J.: Siple Dome ice reveals two modes of millennial  $\text{CO}_2$  change during the last ice age,  
910 *Nature Communications*, 5, doi:10.1038/ncomms4723, 2014.

911 Ahn, J., Brook, E. J., Mitchell, L., Rosen, J., McConnell, J. R., Taylor, K., Etheridge, D., and Rubino, M.:  
912 Atmospheric  $\text{CO}_2$  over the last 1000 years: A high-resolution record from the West Antarctic Ice Sheet  
913 (WAIS) Divide ice core, *Global Biogeochemical Cycles*, 26, <https://doi.org/10.1029/2011GB004247>, 2012.

914 Allen, C. S., Pike, J., and Pudsey, C. J.: Last glacial–interglacial sea-ice cover in the SW Atlantic and its potential  
915 role in global deglaciation, *Quaternary Science Reviews*, 30, 2446–2458, 2011.

916 Archer, D., and Maier-Reimer, E.: Effect of deep-sea sedimentary calcite preservation on atmospheric  $\text{CO}_2$   
917 concentration, *Nature*, 367, 260–263, 1994.

918 Archer, D., Lyle, M., Rodgers, K., and Froelich, P.: What controls opal preservation in tropical deep-sea sediments?,  
919 *Paleoceanography*, 8, 7–21, 1993.

920 Archer, D., Winguth, A., Lea, D., and Mahowald, N.: What caused the glacial/interglacial atmospheric pCO<sub>2</sub>  
921 cycles?, *Reviews of Geophysics*, 38, 159–189, 2000.

922 Audi, G., Bersillon, O., Blachot, J., and Wapstra, A. H.: The Nubase evaluation of nuclear and decay properties,  
923 *Nuclear Physics A*, 729, 3–128, 2003.

924 Bard, E., Raisbeck, G. M., Yiou, F., and Jouzel, J.: Solar modulation of cosmogenic nuclide production over the last  
925 millennium: comparison between <sup>14</sup>C and <sup>10</sup>Be records, *Earth and Planetary Science Letters*, 150, 453–462,  
926 1997.

927 Baumgartner, S., Beer, J., Wagner, G., Kubik, P., Suter, M., Raisbeck, G. M., and Yiou, F.: <sup>10</sup>Be and dust, *Nuclear*  
928 *Instruments and Methods in Physics Research Section B: Beam Interactions with Materials and Atoms*,  
929 123, 296–301, 1997.

930 Baumgartner, S., Beer, J., Masarik, J., Wagner, G., Meynadier, L., and Synal, H.-A.: Geomagnetic Modulation of  
931 the <sup>36</sup>Cl Flux in the GRIP Ice Core, Greenland, *Science*, 279, 1330–1332, 1998.

932 Bauska, T. K., Joos, F., Mix, A. C., Roth, R., Ahn, J., and Brook, E. J.: Links between atmospheric carbon dioxide,  
933 the land carbon reservoir and climate over the past millennium, *Nature Geoscience*, 8, 383–387, 2015.

934 Bé, M.-M., Chisté, V., Dulieu, C., Mougeot, X., Chechev, V., Kondev, F., . . . Wang, B.: Table of Radionuclides  
935 (Comments on evaluations), *Monographic BIPM-5*, 7, 2013.

936 Bereiter, B., Lüthi, D., Siegrist, M., Schüpbach, S., Stocker, T. F., and Fischer, H.: Mode change of millennial CO<sub>2</sub>  
937 variability during the last glacial cycle associated with a bipolar marine carbon seesaw, *Proceedings of the*  
938 *National Academy of Sciences*, 109, 9755–9760, 2012.

939 Berger, A. L.: Long-term variations of daily insolation and Quaternary climatic changes, *Journal of the Atmospheric*  
940 *Sciences*, 35, 2362–2367, 1978.

941 Broecker, W., and Barker, S.: A 190‰ drop in atmosphere's Δ<sup>14</sup>C during the "Mystery Interval" (17.5 to 14.5 kyr),  
942 *Earth and Planetary Science Letters*, 256, 90–99, 2007.

943 Broecker, W. S., and Peng, T.-H.: Gas exchange rates between air and sea, *Tellus*, 26, 21–35, 1974.

944 Bronk Ramsey, C., Staff, R. A., Bryant, C. L., Brock, F., Kitagawa, H., van der Plicht, J., Schlolaut, G., Marshall,  
945 M. H., Brauer, A., Lamb, H. F., Payne, R. L., Tarasov, P. E., Haraguchi, T., Gotanda, K., Yonenobu, H.,  
946 Yokoyama, Y., Tada, R., and Nakagawa, T.: A complete terrestrial radiocarbon record for 11.2 to 52.8 kyr  
947 B.P., *Science*, 338, 370–374, 2012.

948 Brovkin, V., Ganopolski, A., Archer, D., and Munhoven, G.: Glacial CO<sub>2</sub> cycle as a succession of key physical and  
949 biogeochemical processes, *Climate of the Past*, 8, 251–264, 2012.

950 Butzin, M., Köhler, P., and Lohmann, G.: Marine radiocarbon reservoir age simulations for the past 50,000 years,  
951 *Geophysical Research Letters*, 44, 8473–8480, 2017.

952 Buizert, C., Cuffey, K. M., Severinghaus, J. P., Baggenstos, D., Fudge, T. J., Steig, E. J., Markle, B. R., Winstrup,  
953 M., Rhodes, R. H., Brook, E. J., Sowers, T. A., Clow, G. D., Cheng, H., Edwards, R. L., Sigl, M.,  
954 McConnell, J. R., and Taylor, K. C.: The WAIS Divide deep ice core WD2014 chronology – Part 1:

955 Methane synchronization (68-31 ka BP) and the gas age–ice age difference, *Climate of the Past*, 11, 153–  
956 173, 2015.

957 Channell, J. E., Hodell, D. A., Crowhurst, S. J., Skinner, L. C., and Muscheler, R.: Relative paleointensity (RPI) in  
958 the latest Pleistocene (10-45 ka) and implications for deglacial atmospheric radiocarbon, *Quaternary*  
959 *Science Reviews*, 191, 57–72, 2018.

960 Cheng, H., Edwards, R. L., Southon, J., Matsumoto, K., Feinberg, J. M., Sinha, A., . . . Ning, Y.: Atmospheric  
961  $^{14}\text{C}/^{12}\text{C}$  changes during the last glacial period from Hulu Cave, *Science*, 362, 1293–1297, 2018.

962 Delaygue, G., Stocker, T. F., Joos, F., and Plattner, G.-K.: Simulation of atmospheric radiocarbon during abrupt  
963 oceanic circulation changes: trying to reconcile models and reconstructions, *Quaternary Science Reviews*,  
964 22, 1647–1658, 2003.

965 Dlugokencky, E., Lang, P., Mund, J., Crotwell, A., Crotwell, M., and Thoning, K.: Atmospheric Carbon Dioxide  
966 Dry Air Mole Fractions from the NOAA ESRL Carbon Cycle Cooperative Global Air Sampling Network,  
967 1968-2015, Version: 2016-08-30, available at: [ftp://afp.cmdl.noaa.gov/data/trace\\_gases/co2/flask/surface/](ftp://afp.cmdl.noaa.gov/data/trace_gases/co2/flask/surface/)  
968 (last access: 17 August 2016), 2016.

969 Edwards, N. R., and Marsh, R.: Uncertainties due to transport-parameter sensitivity in an efficient 3-D ocean-  
970 climate model, *Climate Dynamics*, 24, 415–433, 2005.

971 Edwards, N. R., Willmott, A. J., and Killworth, P. D.: On the Role of Topography and Wind Stress on the Stability  
972 of the Thermohaline Circulation, *Journal of Physical Oceanography*, 28, 756–778, 1998.

973 Eggleston, S., Schmitt, J., Bereiter, B., Schneider, R., and Fischer, H.: Evolution of the stable carbon isotope  
974 composition of atmospheric  $\text{CO}_2$  over the last glacial cycle, *Paleoceanography*, 31, 434–452, 2016.

975 Elsässer, C., Wagenbach, D., Levin, I., Stanzick, A., Christl, M., Wallner, A., . . . Dibb, J.: Simulating ice core  $^{10}\text{Be}$   
976 on the glacial–interglacial timescale, *Climate of the Past*, 11, 115–133, 2015.

977 Field, C. V., Schmidt, G. A., Koch, D., and Salyk, C.: Modeling production and climate-related impacts on  $^{10}\text{Be}$   
978 concentration in ice cores, *Journal of Geophysical Research: Atmospheres*, 111,  
979 <https://doi.org/10.1029/2005JD006410>, 2006.

980 Finkel, R. C., and Nishiizumi, K.: Beryllium 10 concentrations in the Greenland Ice Sheet Project 2 ice core from 3-  
981 40 ka, *Journal of Geophysical Research: Oceans*, 102, 26699–26706, 1997.

982 Fischer, H., Schmitt, J., Lüthi, D., Stocker, T. F., Tschumi, T., Parekh, P., . . . Wolff, E.: The role of Southern Ocean  
983 processes in orbital and millennial  $\text{CO}_2$  variations – A synthesis, *Quaternary Science Reviews*, 29, 193–  
984 205, 2010.

985 Galbraith, E. D., and Skinner, L. C.: The Biological Pump During the Last Glacial Maximum, *Annual Review of*  
986 *Marine Science*, 12, 559–586, 2020.

987 Ganopolski, A., and Brovkin, V.: Simulation of climate, ice sheets and  $\text{CO}_2$  evolution during the last four glacial  
988 cycles with an Earth system model of intermediate complexity, *Climate of the Past*, 13, 1695–1716, 2017.

989 Gehlen, M., Bopp, L. E., Aumont, O., Heinze, C., and Ragueneau, O.: Reconciling surface ocean productivity,  
990 export fluxes and sediment composition in a global biogeochemical ocean model, *Biogeosciences*, 3, 521–  
991 537, 2006.

992 Gersonde, R., Crosta, X., Abelmann, A., and Armand, L.: Sea-surface temperature and sea ice distribution of the  
993 Southern Ocean at the EPILOG Last Glacial Maximum—a circum-Antarctic view based on siliceous  
994 microfossil records, *Quaternary Science Reviews*, 24, 869–896, 2005.

995 Gkinis, V., Simonsen, S. B., Buchardt, S. L., White, J. W., and Vinther, B. M.: Water isotope diffusion rates from  
996 the NorthGRIP ice core for the last 16,000 years – Glaciological and paleoclimatic implications, *Earth and  
997 Planetary Science Letters*, 405, 132–141, 2014.

998 Griffies, S. M.: The Gent-McWilliams Skew Flux, *Journal of Physical Oceanography*, 28, 831–841, 1998.

999 Hain, M. P., Sigman, D. M., and Haug, G. H.: Distinct roles of the Southern Ocean and North Atlantic in the  
1000 deglacial atmospheric radiocarbon decline, *Earth and Planetary Science Letters*, 394, 198–208, 2014.

1001 Heikkilä, U., Beer, J., and Feichter, J.: Meridional transport and deposition of atmospheric  $^{10}\text{Be}$ , *Atmospheric  
1002 Chemistry and Physics*, 9, 515–527, 2009.

1003 Heikkilä, U., Phipps, S. J., and Smith, A. M.:  $^{10}\text{Be}$  in late deglacial climate simulated by ECHAM5-HAM – Part 1:  
1004 Climatological influences on  $^{10}\text{Be}$  deposition, *Climate of the Past*, 9, 2641–2649, 2013.

1005 Heinze, C., Maier-Reimer, E., Winguth, A. M., and Archer, D.: A global oceanic sediment model for long-term  
1006 climate studies, *Global Biogeochemical Cycles*, 13, 221–250, 1999.

1007 Herbst, K., Muscheler, R., and Heber, B.: The new local interstellar spectra and their influence on the production  
1008 rates of the cosmogenic radionuclides  $^{10}\text{Be}$  and  $^{14}\text{C}$ , *Journal of Geophysical Research: Space Physics*, 122,  
1009 23–34, 2017.

1010 Hoff, U., Rasmussen, T. L., Stein, R., Ezat, M. M., and Fahl, K.: Sea ice and millennial-scale climate variability in  
1011 the Nordic seas 90 kyr ago to present, *Nature Communications*, 7, doi:10.1038/ncomms12247, 2016.

1012 Hughen, K., Lehman, S., Southon, J., Overpeck, J., Marchal, O., Herring, C., and Turnbull, J.:  $^{14}\text{C}$  Activity and  
1013 Global Carbon Cycle Changes over the Past 50,000 Years, *Science*, 303, 202–207, 2004.

1014 Huiskamp, W. N., and Meissner, K. J.: Oceanic carbon and water masses during the Mystery Interval: A model-data  
1015 comparison study, *Paleoceanography and Paleoclimatology*, 27, <https://doi.org/10.1029/2012PA002368>,  
1016 2012.

1017 Jeltsch-Thömmes, A., Battaglia, G., Cartapanis, O., Jaccard, S. L., and Joos, F.: Low terrestrial carbon storage at the  
1018 Last Glacial Maximum: constraints from multi-proxy data, *Climate of the Past*, 15, 849–879, 2019.

1019 Köhler, P., Muscheler, R., and Fischer, H.: A model-based interpretation of low-frequency changes in the carbon  
1020 cycle during the last 120,000 years and its implications for the reconstruction of atmospheric  $\Delta^{14}\text{C}$ ,  
1021 *Geochemistry Geophysics Geosystems*, 7, 1–22, 2006.

1022 Köhler, P., Nehrbass-Ahles, C., Schmitt, J., Stocker, T. F., and Fischer, H.: A 156 kyr smoothed history of the  
1023 atmospheric greenhouse gases  $\text{CO}_2$ ,  $\text{CH}_4$ , and  $\text{N}_2\text{O}$  and their radiative forcing, *Earth System Science Data*,  
1024 9, 363–387, 2017.

1025 Kalnay, E., Kanamitsu, M., Kistler, R., Collins, W., Deaven, D., Gandin, L., . . . Joseph, D.: The NCEP/NCAR 40-  
1026 Year Reanalysis Project, *Bulletin of the American Meteorological Society*, 77, 437–471, 1996.

1027 Key, R. M., Kozyr, A., Sabine, C. L., Lee, K., Wanninkhof, R., Bullister, J. L., . . . Peng, T.-H.: A global ocean  
1028 carbon climatology: Results from Global Data Analysis Project (GLODAP), *Global Biogeochemical*  
1029 *Cycles*, 18, <https://doi.org/10.1029/2004GB002247>, 2004.

1030 Kovaltsov, G. A., and Usoskin, I. G.: A new 3D numerical model of cosmogenic nuclide  $^{10}\text{Be}$  production in the  
1031 atmosphere, *Earth and Planetary Science Letters*, 291, 182–188, 2010.

1032 Krakauer, N. Y., Randerson, J. T., Primeau, F. W., Gruber, N., and Menemenlis, D.: Carbon isotope evidence for the  
1033 latitudinal distribution and wind speed dependence of the air-sea gas transfer velocity, *Tellus B: Chemical*  
1034 *and Physical Meteorology*, 58, 390–417, 2006.

1035 Kukla, G., and Robinson, D.: Annual Cycle of Surface Albedo, *Monthly Weather Review*, 108, 56–68, 1980.

1036 Laj, C., Kissel, C., Mazaud, A., Channell, J. E., and Beer, J.: North Atlantic palaeointensity stack since 75ka  
1037 (NAPIS-75) and the duration of the Laschamp event, *Philosophical Transactions of the Royal Society of*  
1038 *London. Series A: Mathematical, Physical and Engineering Sciences*, 358, 1009–1025, 2000.

1039 Laj, C., Kissel, C., Mazaud, A., Michel, E., Muscheler, R., and Beer, J.: Geomagnetic field intensity, North Atlantic  
1040 Deep Water circulation and atmospheric  $\Delta^{14}\text{C}$  during the last 50 kyr, *Earth and Planetary Science Letters*,  
1041 200, 177–190, 2002.

1042 Laj, C., Kissel, C., and Beer, J.: High resolution global paleointensity stack since 75 kyr (GLOPIS-75) calibrated to  
1043 absolute values, *Timescales of the Paleomagnetic Field*, 145, 255–265, 2004.

1044 Laj, C., Guillou, H., and Kissel, C.: Dynamics of the earth magnetic field in the 10–75 kyr period comprising the  
1045 Laschamp and Mono Lake excursions: New results from the French Chaîne des Puys in a global  
1046 perspective, *Earth and Planetary Science Letters*, 387, 184–197, 2014.

1047 Lisiecki, L. E., and Stern, J. V.: Regional and global benthic  $\delta^{18}\text{O}$  stacks for the last glacial cycle,  
1048 *Paleoceanography*, 31, 1368–1394, 2016.

1049 Laurantou, A., Chappellaz, J., Barnola, J.-M., Masson-Delmotte, V., and Raynaud, D.: Changes in atmospheric  $\text{CO}_2$   
1050 and its carbon isotopic ratio during the penultimate deglaciation, *Quaternary Science Reviews*, 29, 1983–  
1051 1992, 2010.

1052 Lüthi, D., Bereiter, B., Stauffer, B., Winkler, R., Schwander, J., Kindler, P., Leuenberger, M., Kipfstuhl, S., Capron,  
1053 E., Landais, A., Fischer, H., and Stocker, T. F.:  $\text{CO}_2$  and  $\text{O}_2/\text{N}_2$  variations in and just below the bubble-  
1054 clathrate transformation zone of Antarctic ice cores, *Earth and Planetary Science Letters*, 297, 226–233,  
1055 2010.

1056 MacFarling-Meure, C., Etheridge, D., Trudinger, C., Langenfelds, R., van Ommen, T., Smith, A., and Elkins, J.:  
1057 Law Dome  $\text{CO}_2$ ,  $\text{CH}_4$  and  $\text{N}_2\text{O}$  ice core records extended to 2000 years BP, *Geophysical Research Letters*,  
1058 33, <https://doi.org/10.1029/2006GL026152>, 2006.

1059 Marcott, S. A., Bauska, T. K., Buizert, C., Steig, E. J., Rosen, J. L., Cuffey, K. M., Fudge, T. J., Severinghaus, J. P.,  
1060 Ahn, J., Kalk, M. L., McConnell, J. R., Sowers, T., Taylor, K. C., White, J. W., and Brook, E. J.:  
1061 Centennial Scale Changes in the Global Carbon Cycle During the Last Deglaciation, *Nature*, 514, 616–619,  
1062 2014.

1063 Monnin, E., Indermühle, A., Dällenbach, A., Flückiger, J., Stauffer, B., Stocker, T. F., Raynaud, D., and Barnola, J.-  
1064 M.: Atmospheric CO<sub>2</sub> concentrations over the last glacial termination, *Science*, 291, 112–114, 2001.

1065 Monnin, E., Steig, E. J., Siegenthaler, U., Kawamura, K., Schwander, J., Stauffer, B., Stocker, T. F., Morse, D. L.,  
1066 Barnola, J.-M., Bellier, B., Raynaud, D., and Fischer, H.: Evidence for substantial accumulation rate  
1067 variability in Antarctica during the Holocene, through synchronization of CO<sub>2</sub> in the Taylor Dome, Dome  
1068 C and DML ice cores, *Earth and Planetary Science Letters*, 224, 45–54, 2004.

1069 Müller, J., and Stein, R.: High-resolution record of late glacial and deglacial sea ice changes in Fram Strait  
1070 corroborates ice–ocean interactions during abrupt climate shifts, *Earth and Planetary Science Letters*, 403,  
1071 446–455, 2014.

1072 Müller, S. A., Joos, F., Edwards, N. R., and Stocker, T. F.: Water Mass Distribution and Ventilation Time Scales in  
1073 a Cost-Efficient, Three-Dimensional Ocean Model, *Journal of Climate*, 19, 5479–5499, 2006.

1074 Müller, S. A., Joos, F., Plattner, G.-K., Edwards, N. R., and Stocker, T. F.: Modeled natural and excess radiocarbon:  
1075 Sensitivities to the gas exchange formulation and ocean transport strength, *Global Biogeochemical Cycles*,  
1076 22, <https://doi.org/10.1029/2007GB003065>, 2008.

1077 Marchal, O., Stocker, T. F., and Muscheler, R.: Atmospheric radiocarbon during the Younger Dryas: production,  
1078 ventilation, or both?, *Earth and Planetary Science Letters*, 185, 383–395, 2001.

1079 Mariotti, V., Paillard, D., Bopp, L., Roche, D. M., and Bouttes, N.: A coupled model for carbon and radiocarbon  
1080 evolution during the last deglaciation, *Geophysical Research Letters*, 43, 1306–1313, 2016.

1081 Masarik, J., and Beer, J.: Simulation of particle fluxes and cosmogenic nuclide production in the Earth's atmosphere,  
1082 *Journal of Geophysical Research: Atmospheres*, 104, 12099–12111, 1999.

1083 Masarik, J., and Beer, J.: An updated simulation of particle fluxes and cosmogenic nuclide production in the Earth's  
1084 atmosphere, *Journal of Geophysical Research: Atmospheres*, 114, <https://doi.org/10.1029/2008JD010557>,  
1085 2009.

1086 Menviel, L., Joos, F., and Ritz, S. P.: Simulating atmospheric CO<sub>2</sub>, <sup>13</sup>C and the marine carbon cycle during the Last  
1087 Glacial–Interglacial cycle: possible role for a deepening of the mean remineralization depth and an increase  
1088 in the oceanic nutrient inventory, *Quaternary Science Reviews*, 56, 46–68, 2012.

1089 Muscheler, R., and Heikkilä, U.: Constraints on long-term changes in solar activity from the range of variability of  
1090 cosmogenic radionuclide records, *Astrophysics and Space Sciences Transactions*, 7, 355–364, 2011.

1091 Muscheler, R., Beer, J., Wagner, G., Laj, C., Kissel, C., Raisbeck, G. M., . . . Kubike, P. W.: Changes in the carbon  
1092 cycle during the last deglaciation as indicated by the comparison of <sup>10</sup>Be and <sup>14</sup>C records, *Earth and  
1093 Planetary Science Letters*, 219, 325–340, 2004.

1094 Muscheler, R., Adolphi, F., Herbst, K., and Nilsson, A.: The Revised Sunspot Record in Comparison to Cosmogenic  
1095 Radionuclide-Based Solar Activity Reconstructions, *Solar Physics*, 291, 3025–3043, 2016.

1096 Nowaczyk, N. R., Arz, H. W., Frank, U., Kind, J., and Plessen, B.: Dynamics of the Laschamp geomagnetic  
1097 excursion from Black Sea sediments, *Earth and Planetary Science Letters*, 351–352, 54–69, 2012.

1098 Nowaczyk, N. R., Frank, U., Kind, J., and Arz, H. W.: A high-resolution paleointensity stack of the past 14 to 68 ka  
1099 from Black Sea sediments, *Earth and Planetary Science Letters*, 384, 1–16, 2013.

1100 Orr, J. C., Najjar, R. G., Aumont, O., Bopp, L., Bullister, J. L., Danabasoglu, G., . . . Yool, A.: Biogeochemical  
1101 protocols and diagnostics for the CMIP6 Ocean Model Intercomparison Project (OMIP), *Geoscientific*  
1102 *Model Development*, 10, 2169–2199, 2017.

1103 Parekh, P., Joos, F., and Müller, S. A.: A modeling assessment of the interplay between aeolian iron fluxes and iron-  
1104 binding ligands in controlling carbon dioxide fluctuations during Antarctic warm events, *Paleoceanography*  
1105 and *Paleoclimatology*, 23, <https://doi.org/10.1029/2007PA001531>, 2008.

1106 Peltier, W. R.: Ice Age Paleotopography, *Science*, 265, 195–201, 1994.

1107 Poluianov, S. V., Kovaltsov, G. A., Mishev, A. L., and Usoskin, I. G.: Production of cosmogenic isotopes  $^7\text{Be}$ ,  $^{10}\text{Be}$ ,  
1108  $^{14}\text{C}$ ,  $^{22}\text{Na}$ , and  $^{36}\text{Cl}$  in the atmosphere: Altitudinal profiles of yield functions, *Journal of Geophysical*  
1109 *Research: Atmospheres*, 121, 8125–8136, 2016.

1110 Potgieter, M. S., Vos, E. E., Boezio, M., De Simone, N., Di Felice, V., and Formato, V.: Modulation of Galactic  
1111 Protons in the Heliosphere During the Unusual Solar Minimum of 2006 to 2009, *Solar Physics*, 289, 391–  
1112 406, 2014.

1113 Primeau, F.: Characterizing Transport between the Surface Mixed Layer and the Ocean Interior with a Forward and  
1114 Adjoint Global Ocean Transport Model, *Journal of Physical Oceanography*, 35, 545–564, 2005.

1115 Raisbeck, G. M., Cauquoin, A., Jouzel, J., Landais, A., Petit, J.-R., Lipenkov, V. Y., . . . Yiou, F.: An improved  
1116 north-south synchronization of ice core records around the 41 kyr  $^{10}\text{Be}$  peak, *Climate of the Past*, 13, 217–  
1117 229, 2017.

1118 Rasmussen, S. O., Abbott, P. M., Blunier, T., Bourne, A. J., Brook, E. J., Buchardt, S. L., . . . Winstrup, M.: A first  
1119 chronology for the North Greenland Eemian Ice Drilling (NEEM) ice core, *Climate of the Past*, 9, 2713–  
1120 2730, 2013.

1121 Reimer, P., Bard, E., Bayliss, A., Beck, J., Blackwell, P., Ramsey, C., . . . Van der Plicht, J.: IntCal13 and Marine13  
1122 Radiocarbon Age Calibration Curves 0-50,000 Years cal BP, *Radiocarbon*, 55, 1869–1887, 2013.

1123 Reimer, P., Austin, W.E.N., Bard, E., Bayliss, A., Blackwell, P. G., Ramsey, C. B., . . . Talamo, S.: The IntCal20  
1124 Northern Hemisphere radiocarbon age calibration curve (0-55 kcal BP), *Radiocarbon*, in press.

1125 Ritz, S. P., Stocker, T. F., and Joos, F.: A Coupled Dynamical Ocean–Energy Balance Atmosphere Model for  
1126 Paleoclimate Studies, *Journal of Climate*, 24, 349–375, 2011.

1127 Roth, R., and Joos, F.: A reconstruction of radiocarbon production and total solar irradiance from the Holocene  $^{14}\text{C}$   
1128 and  $\text{CO}_2$  records: implications of data and model uncertainties, *Climate of the Past*, 9, 1879–1909, 2013.

1129 Roth, R., Ritz, S. P., and Joos, F.: Burial-nutrient feedbacks amplify the sensitivity of atmospheric carbon dioxide to  
1130 changes in organic matter remineralisation, *Earth System Dynamics*, 5, 321–343, 2014.

1131 Rubino, M., Etheridge, D. M., Trudinger, C. M., Allison, C. E., Battle, M. O., Langenfelds, R. L., Steele, L. P.,  
1132 Curran, M., Bender, M., White, J. W. C., Jenk, T. M., Blunier, T., and Francey, R. J.: A revised 1000-year  
1133 atmospheric  $\delta^{13}\text{C}$ - $\text{CO}_2$  record from Law Dome and South Pole, Antarctica, *Journal of Geophysical*  
1134 *Research: Atmospheres*, 118, 8482–8499, 2013.

1135 Sarinthein, M., Schneider, B., and Grootes, P. M.: Peak glacial  $^{14}\text{C}$  ventilation ages suggest major draw-down of  
1136 carbon into the abyssal ocean, *Climate of the Past*, 9, 2595–2614, 2013.

1137 Schneider, R., Schmitt, J., Köhler, P., Joos, F., and Fischer, H.: A reconstruction of atmospheric carbon dioxide and  
1138 its stable carbon isotopic composition from the penultimate glacial maximum to the last glacial inception,  
1139 *Climate of the Past*, 9, 2507–2523, 2013.

1140 Siegenthaler, U., and Oeschger, H.: Biospheric CO<sub>2</sub> emissions during the past 200 years reconstructed by  
1141 deconvolution of ice core data, *Tellus*, 39B, 140–154, 1987.

1142 Siegenthaler, U., Heimann, M., and Oeschger, H.: <sup>14</sup>C Variations Caused by Changes in the Global Carbon Cycle,  
1143 *Radiocarbon*, 22, 177–191, 1980.

1144 Sigl, M., Fudge, T. J., Winstrup, M., Cole-Dai, J., Ferris, D., McConnell, J. R., Taylor, K. C., Welten, K. C.,  
1145 Woodruff, T. E., Adolphi, F., Bisiaux, M., Brook, E. J., Buizert, C., Caffee, M. W., Dunbar, N. W.,  
1146 Edwards, R., Geng, L., Iverson, N., Koffman, B., Layman, L., Maselli, O. J., McGwire, K., Muscheler, R.,  
1147 Nishiizumi, K., Pasteris, D. R., Rhodes, R. H., and Sowers, T. A.: The WAIS Divide deep ice core  
1148 WD2014 chronology – Part 2: Annual-layer counting (0–31 ka BP), *Climate of the Past*, 12, 769–786, 2016.

1149 Skinner, L. C., Fallon, S., Waelbroeck, C., Michel, E., and Barker, S.: Ventilation of the Deep Southern Ocean and  
1150 Deglacial CO<sub>2</sub> Rise, *Science*, 328, 1147–1151, 2010.

1151 Skinner, L. C., Primeau, F., Freeman, E., de la Fuente, M., Goodwin, P. A., Gottschalk, J., . . . Scrivner, A. E.:  
1152 Radiocarbon constraints on the glacial ocean circulation and its impact on atmospheric CO<sub>2</sub>, *Nature*  
1153 *Communications*, 8, doi:10.1038/ncomms16010, 2017.

1154 Skinner, L. C., Muschitiello, F., and Scrivner, A. E.: Marine Reservoir Age Variability Over the Last Deglaciation:  
1155 Implications for Marine Carbon Cycling and Prospects for Regional Radiocarbon Calibrations,  
1156 *Paleoceanography and Paleoclimatology*, 34, 1807–1815, 2019.

1157 Soulet, G., Skinner, L. C., Beaupré, S. R., and Galy, V.: A Note on Reporting of Reservoir <sup>14</sup>C Disequilibria and  
1158 Age Offsets, *Radiocarbon*, 58, 205–211, 2016.

1159 Southon, J., Noronha, A. L., Cheng, H., Edwards, R. L., and Wang, Y.: A high-resolution record of atmospheric <sup>14</sup>C  
1160 based on Hulu Cave speleothem H82, *Quaternary Science Reviews*, 33, 32–41, 2012.

1161 Stuiver, M., and Polach, H. A.: Discussion: Reporting of <sup>14</sup>C Data, *Radiocarbon*, 19, 355–363, 1977.

1162 Tschumi, T., Joos, F., and Parekh, P.: How important are Southern Hemisphere wind changes for low glacial carbon  
1163 dioxide? A model study, *Paleoceanography and Paleoclimatology*, 23,  
1164 <https://doi.org/10.1029/2008PA001592>, 2008.

1165 Tschumi, T., Joos, F., Gehlen, M., and Heinze, C.: Deep ocean ventilation, carbon isotopes, marine sedimentation  
1166 and the deglacial CO<sub>2</sub> rise, *Climate of the Past*, 7, 771–800, 2011.

1167 Usoskin, I. G., Hulot, G., Gallet, Y., Roth, R., Licht, A., Joos, F., . . . Khokhlov, A.: Evidence for distinct modes of  
1168 solar activity, *Astronomy & Astrophysics*, 562, 1–4, 2014.

1169 Wagner, G., Beer, J., Masarik, J., Muscheler, R., Kubik, P. W., Mende, W., . . . Yiou, F.: Presence of the solar de  
1170 Vries cycle (~205 years) during the last ice age, *Geophysical Research Letters*, 28, 303–306, 2001.

1171 Wallmann, K., Schneider, B., and Sarnthein, M.: Effects of eustatic sea-level change, ocean dynamics, and nutrient  
1172 utilization on atmospheric pCO<sub>2</sub> and seawater composition over the last 130 000 years: a model study,  
1173 *Climate of the Past*, 12, 339–375, 2016.



1174 Yiou, F., Raisbeck, G. M., Baumgartner, S., Beer, J., Hammer, C., Johnsen, S., . . . Yiou, P.: Beryllium 10 in the  
1175 Greenland Ice Core Project ice core at Summit, Greenland, *Journal of Geophysical Research: Oceans*, 102,  
1176 26783–26794, 1997.

1177

1178

1179

1180

1181

1182

1183

1184

1185

1186

1187

1188

1189

1190

1191

1192

1193

1194

1195

1196

1197

1198

1199

1200

1201

1202

1203

1204

1205

1206

1207

1208

1209

1210

1211

1212

1213 Table 1. Summary of model scenarios considered in this study. Initial conditions refer to the boundary conditions used  
 1214 for the precursor spin-up simulation needed to initialize the transient simulation. These correspond either to  
 1215 preindustrial (PI) or last glacial conditions. The paleoclimate forcing fields, i.e., Orb-GHG-Ice, are reconstructed  
 1216 changes in orbital parameters (Berger, 1978), greenhouse gas radiative forcing based on reconstructed atmospheric  
 1217 greenhouse gas histories (Köhler et al., 2017), and varying ice sheet extent scaled using the global benthic  $\delta^{18}\text{O}$  stack  
 1218 of Lisiecki and Stern (2016). Numbers refer to the scale factor values applied to the tunable model parameters  $\tau$  (wind  
 1219 stress scale factor),  $K_V$  (vertical diffusivity),  $k_w$  (gas transfer velocity),  $rr$  ( $\text{CaCO}_3$ -to-POC export ratio), and  $\ell_{POC}$   
 1220 (POC remineralization length scale) at the last glacial maximum (LGM). These values were chosen in order to achieve  
 1221 an atmospheric  $\text{CO}_2$  concentration close to the LGM level, and are varied over time using the global benthic  $\delta^{18}\text{O}$   
 1222 stack. See Roth et al. (2014) for the Bern3D model parameter set. In all scenarios, the fully coupled model  
 1223 configuration, including the major global carbon reservoirs (atmosphere, terrestrial biosphere, ocean, and sediments),  
 1224 is used.

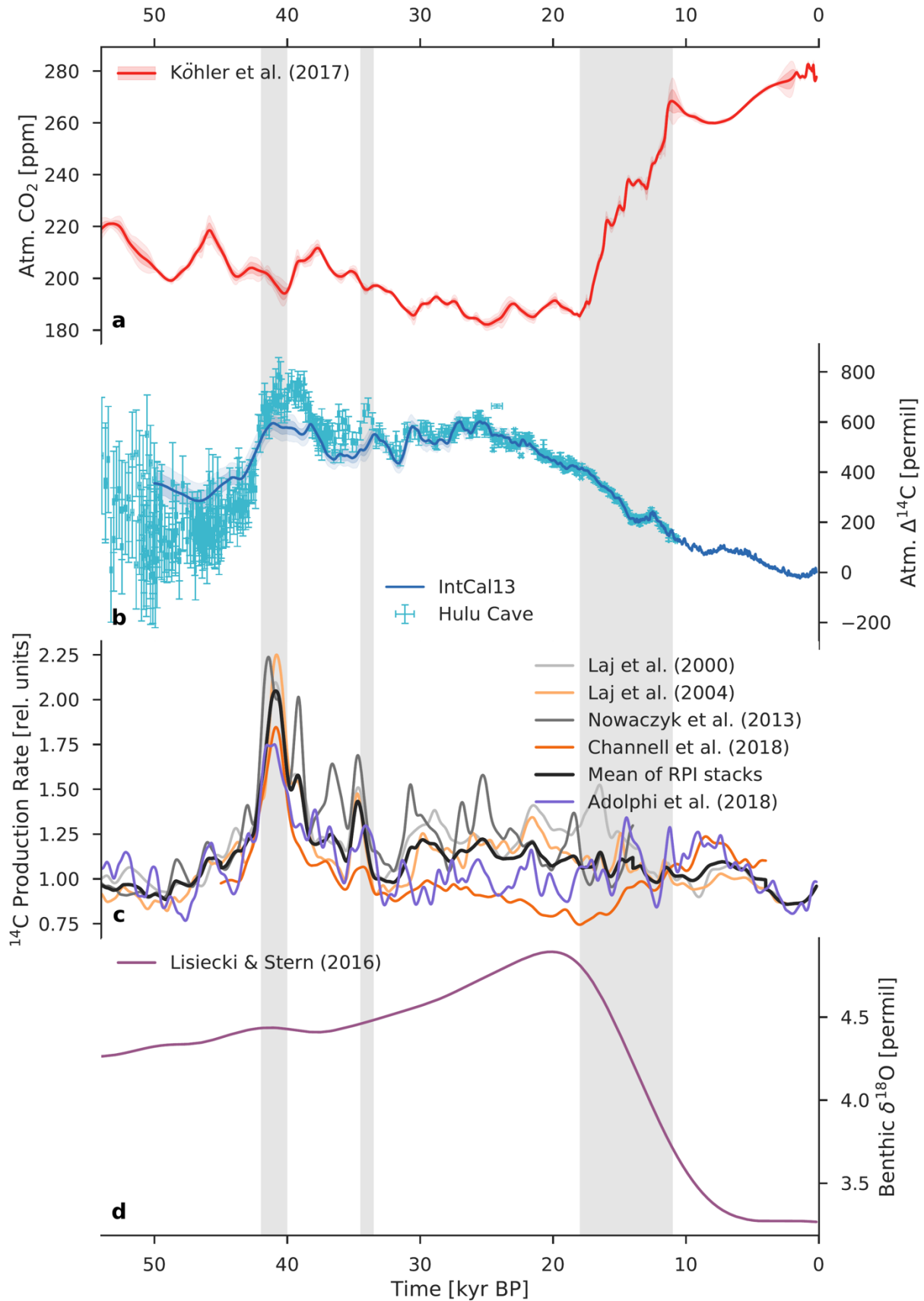
Scenario	Initial conditions	Paleoclimate forcing	Tunable parameters: scale factor at LGM				
			$\tau$	$K_V$	$k_w$	$rr$	$\ell_{POC}$
MOD	PI	-	-	-	-	-	-
PAL	Glacial	Orb-GHG-Ice	-	-	-	-	-
CIRC	Glacial	Orb-GHG-Ice	0.4	0.4	-	-	-
VENT	Glacial	Orb-GHG-Ice	0.4	0.4	0.4	-	-
VENTx	Glacial	Orb-GHG-Ice	0.4	0.4	0.0	-	-
BIO	Glacial	Orb-GHG-Ice	-	-	-	0.8	1.2
PHYS-BIO	Glacial	Orb-GHG-Ice	0.7	0.7	0.7	0.7	-
PHYS-BIOx	Glacial	Orb-GHG-Ice	0.8	0.8	0.8	0.8	1.2

1225  
 1226  
 1227  
 1228  
 1229  
 1230  
 1231  
 1232  
 1233  
 1234  
 1235

1236 Table 2. Production rate estimates in relative units inferred from three fundamentally different reconstruction methods:  
 1237 geomagnetic field data from marine sediments,  $^{10}\text{Be}$  and  $^{36}\text{Cl}$  measurements in polar ice cores, and model-based  
 1238 deconvolution of atmospheric  $\Delta^{14}\text{C}$ . Laj00, Laj04, Now13, and Chn18 refer to the paleointensity-based reconstructions  
 1239 of Laj et al. (2000), Laj et al. (2004), Nowaczyk et al. (2013), and Channell et al. (2018), respectively. Adp18 refers  
 1240 to the ice-core  $^{10}\text{Be}$ -based reconstruction of Adolphi et al. (2018). Int13 and Hul18 refer to the model-based  
 1241 reconstructions from this study, using the IntCal13 calibration curve (Reimer et al., 2013) and the new Hulu Cave  
 1242  $\Delta^{14}\text{C}$  dataset (Cheng et al., 2018). The bold numbers show the mean production rates during the last glacial (50 to 18  
 1243 kyr BP).

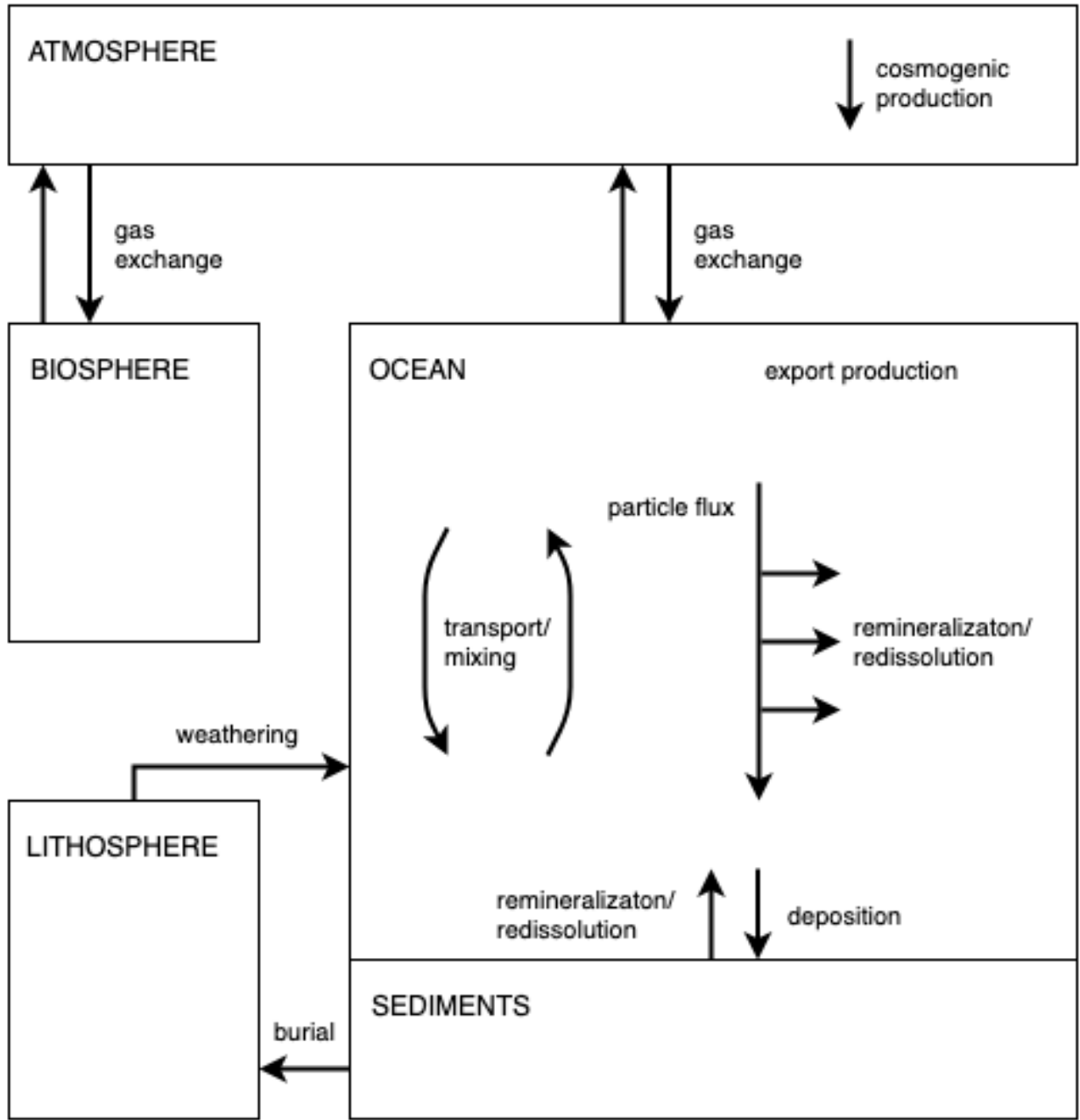
Time (kyr BP)	Mean production rate (relative units)						
	Laj00	Laj04	Now13	Chn18	Adp18	Int13	Hul18
50 to 42	1.08	1.04	1.12	1.08	1.01	1.23	1.14
42 to 37	1.57	1.56	1.71	1.36	1.44	1.45	1.67
37 to 32	1.19	1.09	1.35	0.98	1.10	1.25	1.28
32 to 22	1.22	1.15	1.29	0.92	0.99	1.31	1.31
22 to 18	1.31	1.20	1.17	0.81	0.98	1.11	1.11
<b>50 to 18</b>	<b>1.25</b>	<b>1.18</b>	<b>1.31</b>	<b>1.01</b>	<b>1.08</b>	<b>1.28</b>	<b>1.29</b>

1244  
 1245  
 1246  
 1247  
 1248  
 1249  
 1250  
 1251  
 1252  
 1253  
 1254  
 1255  
 1256  
 1257  
 1258  
 1259  
 1260



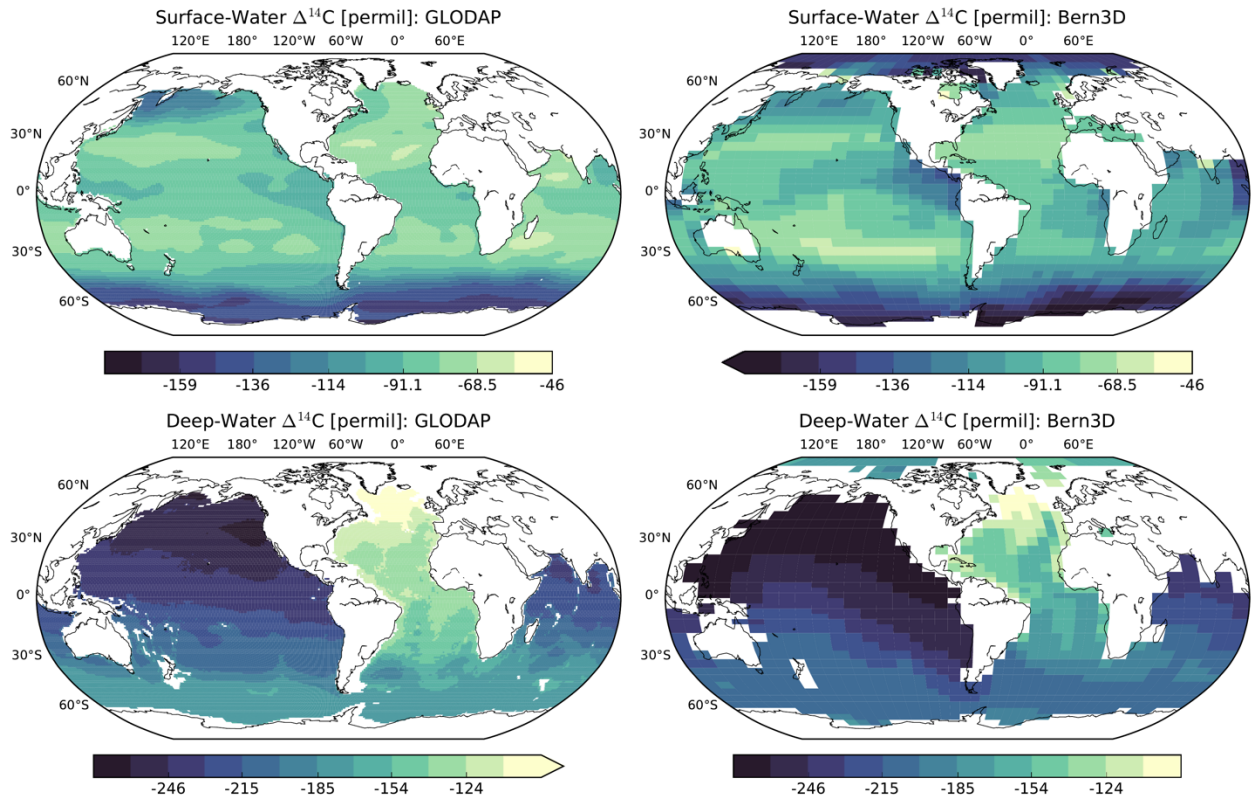
1262 Fig. 1. Comparison of various paleoclimate records for the last 54 kyr. (a) Atmospheric CO<sub>2</sub> from the data compilation  
1263 of Köhler et al. (2017). The light red envelope shows the uncertainty (2σ). (b) Atmospheric Δ<sup>14</sup>C reconstructed from  
1264 <sup>14</sup>C measurements on tree rings, plant macrofossils, speleothems, corals, and foraminifera. The light blue envelope  
1265 shows the uncertainty (2σ) in the IntCal13 calibration curve (Reimer et al., 2013), whereas the Hulu Cave data (Cheng  
1266 et al., 2018) are shown with error bars (1σ). Hulu Cave data are consistent with IntCal13 between ~10.6 and 33.3 kyr  
1267 BP. For both records Δ<sup>14</sup>C values were adjusted to the presently accepted value of the radiocarbon half-life (5700  
1268 years). (c) <sup>14</sup>C production rate in relative units reconstructed from paleointensity data (Laj et al., 2000; Laj et al., 2004;  
1269 Nowaczyk et al., 2013; Channell et al., 2018) and from polar ice-core <sup>10</sup>Be fluxes (Adolphi et al., 2018). The heavy  
1270 dark gray line is the mean paleointensity-based <sup>14</sup>C production rate. (d) Global benthic δ<sup>18</sup>O stack, a proxy for ice  
1271 volume, from Lisiecki and Stern (2016). Three vertical light gray bars indicate the Laschamp excursion (~41 kyr BP),  
1272 when the Earth's geomagnetic dipole field intensity was close to zero, the Mono Lake geomagnetic excursion (~34  
1273 kyr BP), and the last glacial termination (~18 to 11 kyr BP), respectively.

1274  
1275  
1276  
1277  
1278  
1279  
1280  
1281  
1282  
1283  
1284  
1285  
1286  
1287  
1288  
1289  
1290



1291  
 1292 Fig. 2. Schematic diagram of the Bern3D carbon cycle model. The fully coupled model includes the major global  
 1293 carbon reservoirs (atmosphere, terrestrial biosphere, ocean, and sediments) and the exchange fluxes between them.  
 1294 Biogeochemical processes, namely, air-sea gas exchange, biological export production, and particle flux through the  
 1295 water column, are parameterized by refined OCMIP-2 formulations. Details concerning the model are provided in  
 1296 Sect. 2 and Appendix A.

1297  
 1298



1299

1300

1301

Fig. 3. Steady-state distribution of  $\Delta^{14}\text{C}$  in the surface ( $< 100\text{ m}$ ) and deep ( $> 1500\text{ m}$ ) ocean for the preindustrial control run (right), compared to the distribution of  $\Delta^{14}\text{C}$  based on the Global Ocean Data Analysis Project (GLODAP).

1302

1303

1304

1305

1306

1307

1308

1309

1310

1311

1312

1313

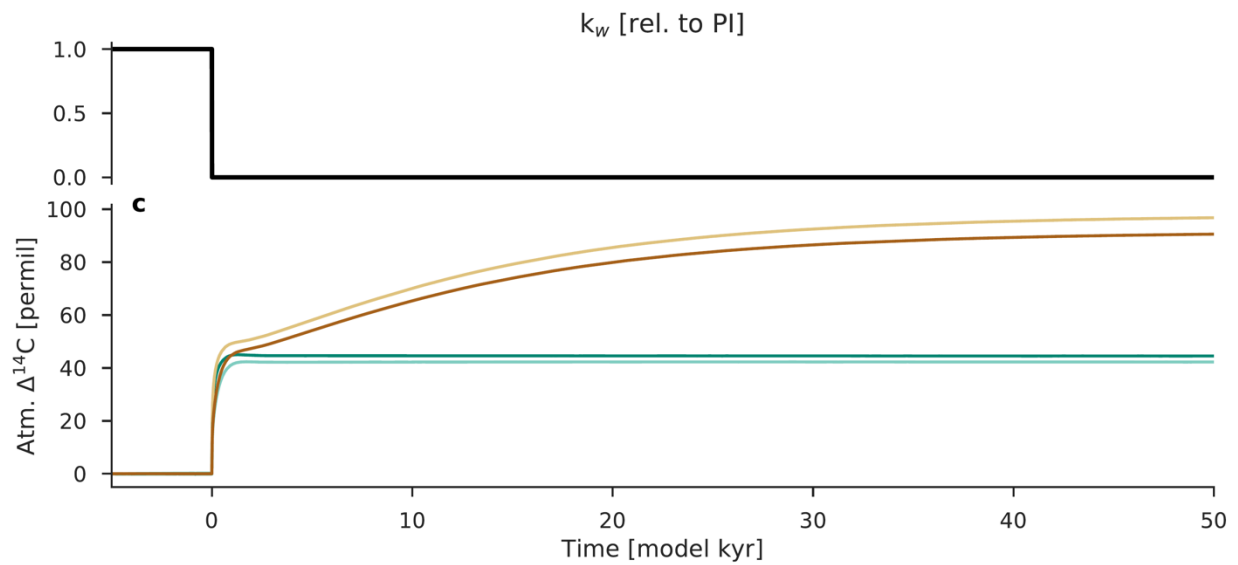
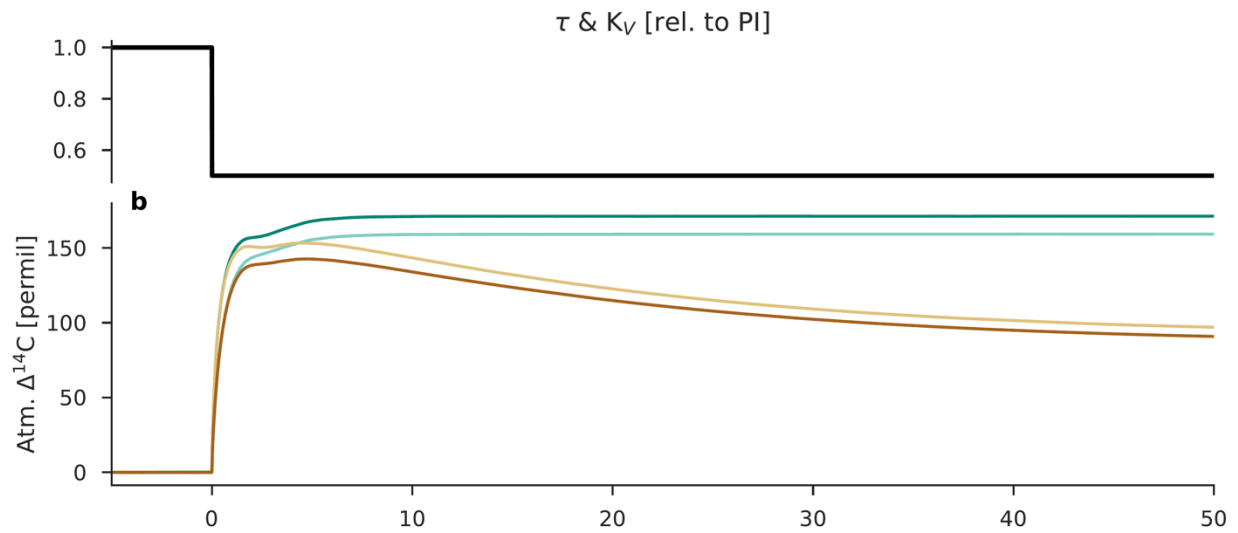
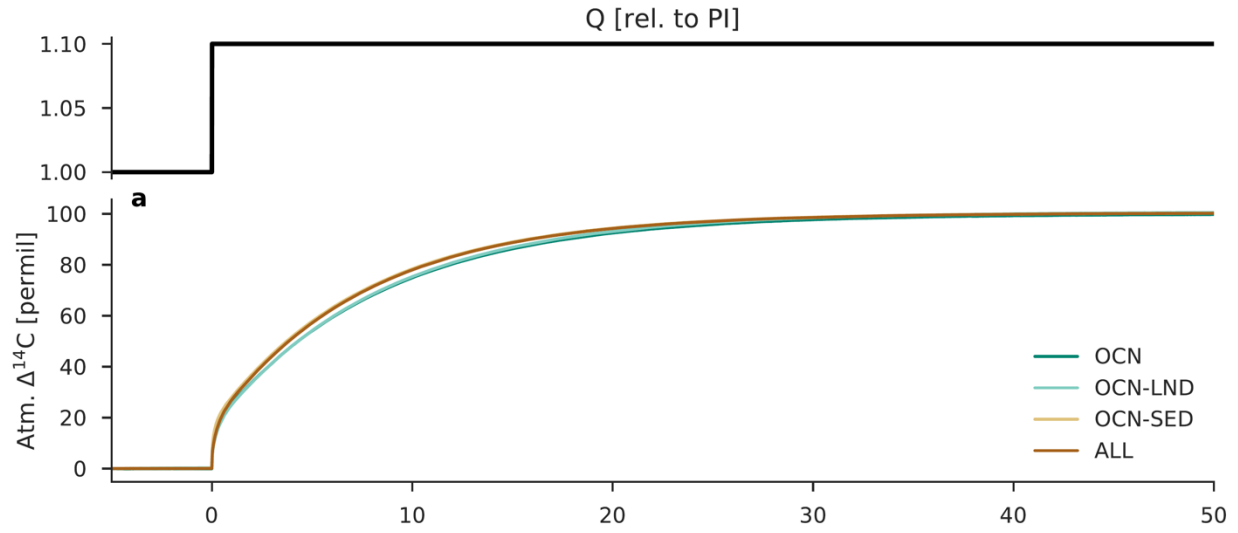
1314

1315

1316

1317

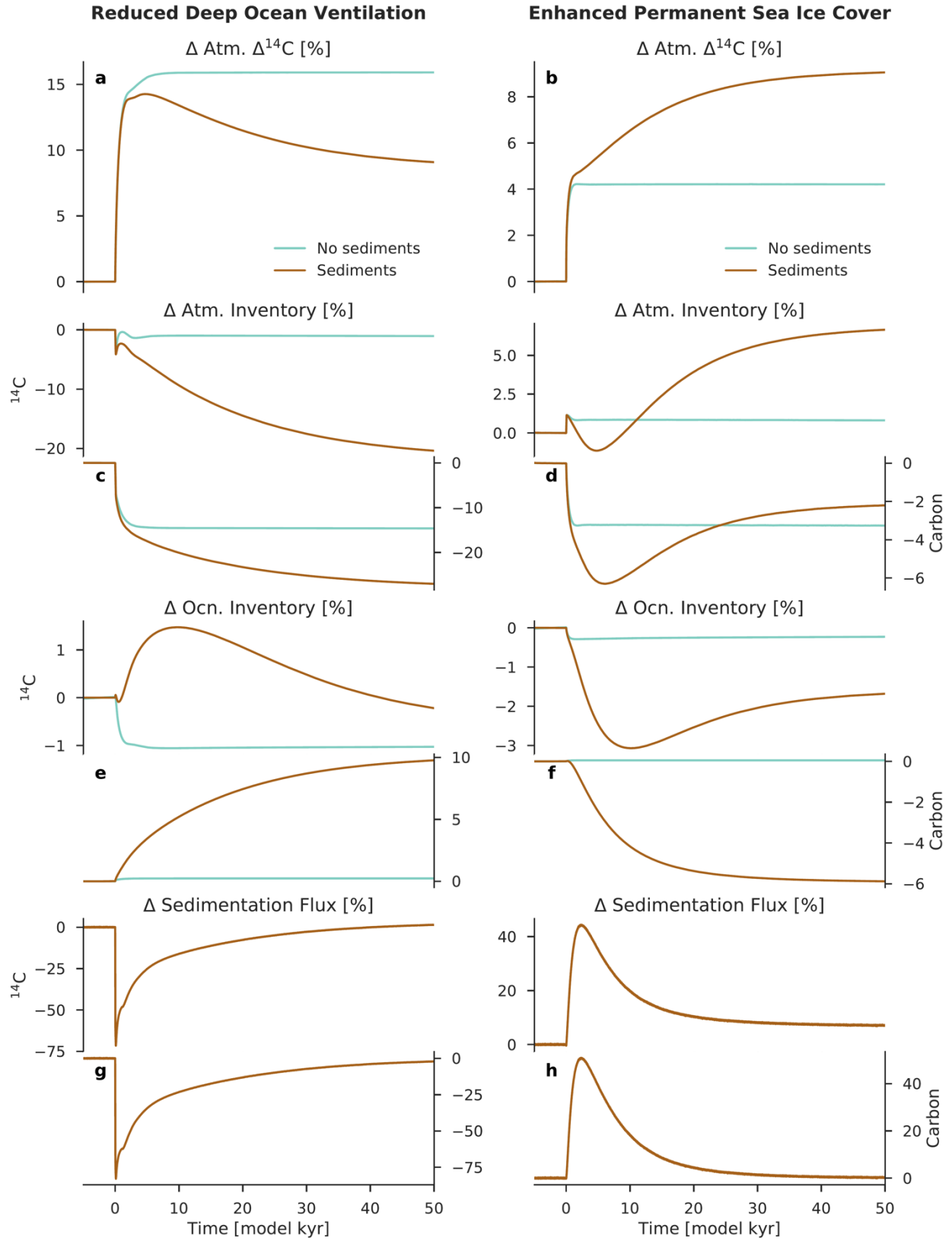
1318





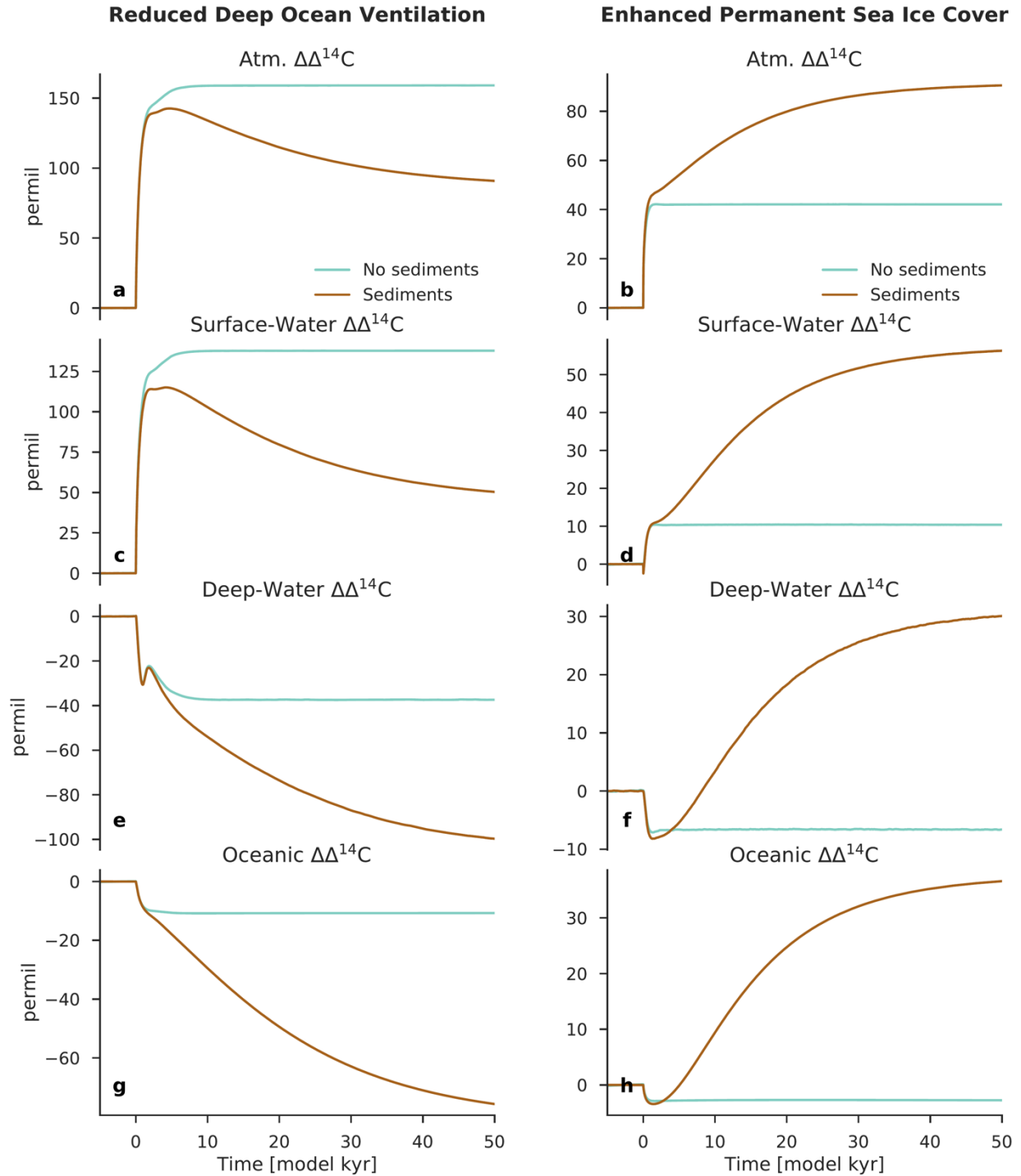
1320 Fig. 4. Response of atmospheric  $\Delta^{14}\text{C}$  to step changes in  $^{14}\text{C}$  production, followed by step changes in the tunable model  
1321 parameters of the ocean carbon cycle. (a)  $^{14}\text{C}$  production  $Q$  is increased at time 0 from 100 to 110 percent of its  
1322 preindustrial value (“higher production” scenario). (b) Wind stress scale factor  $\tau$  and vertical diffusivity  $K_V$  are  
1323 decreased at time 0 from 100 to 50 percent of their preindustrial values (“reduced deep ocean ventilation” scenario).  
1324 (c) Gas transfer velocity  $k_w$  is decreased at time 0 from 100 to 0 percent of its preindustrial value at the north ( $> 60^\circ\text{N}$ )  
1325 and south ( $> 48^\circ\text{S}$ ) poles (“enhanced permanent sea ice cover” scenario). Four model configurations are considered.  
1326 The dark turquoise line shows the model results using the atmosphere–ocean (OCN) configuration, the light turquoise  
1327 line is the atmosphere–ocean–land (OCN-LND) configuration, the light brown line is the atmosphere–ocean–sediment  
1328 (OCN-SED) configuration, and the dark brown line is the atmosphere–ocean–land–sediment (ALL) configuration.

1329  
1330  
1331  
1332  
1333  
1334  
1335  
1336  
1337  
1338  
1339  
1340  
1341  
1342  
1343  
1344  
1345  
1346  
1347  
1348



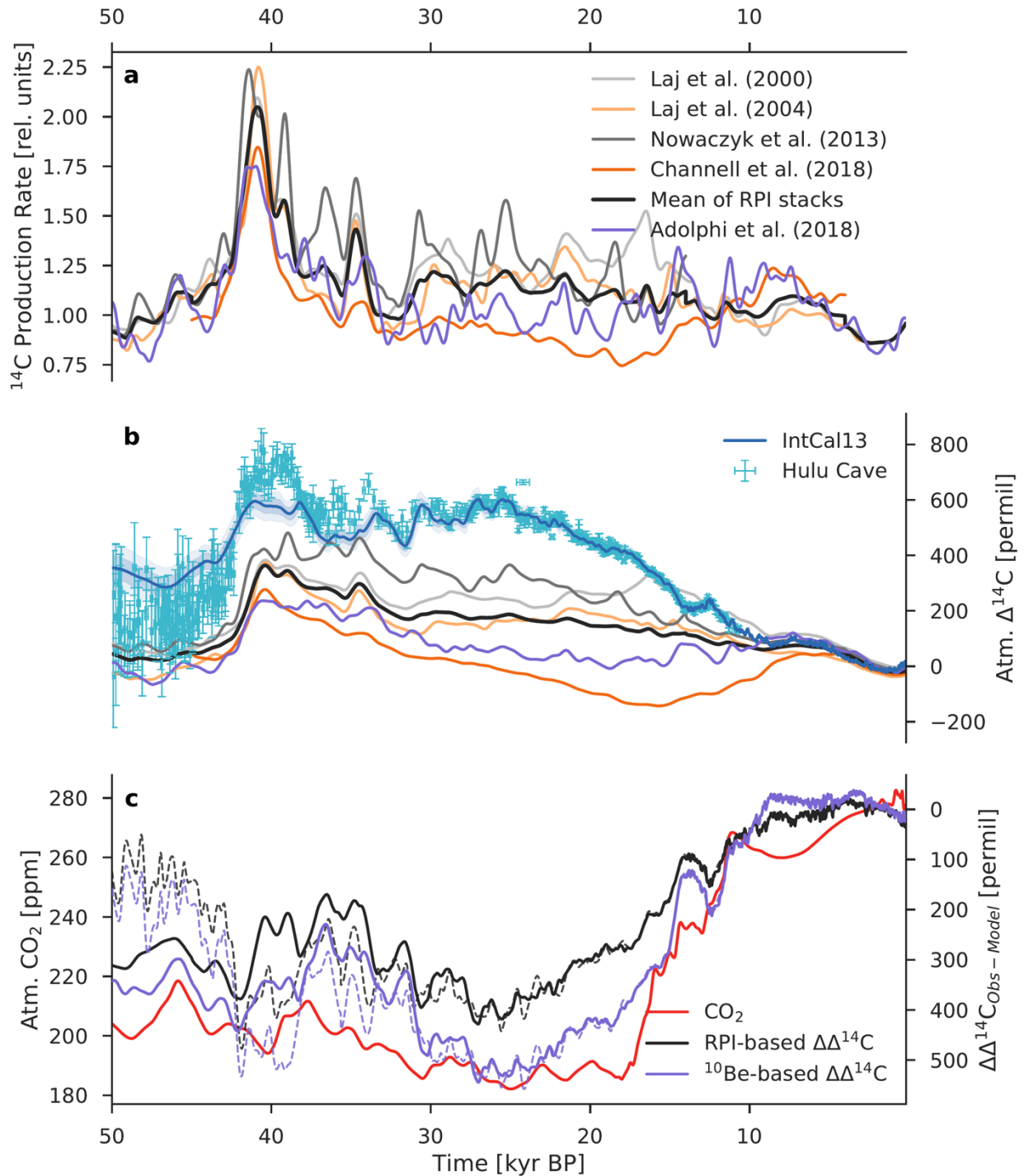
1350 Fig. 5. Changes in carbon reservoir sizes and the sedimentation flux for the scenarios “reduced deep ocean ventilation”  
1351 (left) and “enhanced permanent sea ice cover” (right). The change in atmospheric  $\Delta^{14}\text{C}$  is also shown (a, b). Anomalies  
1352 are expressed here as differences relative to the preindustrial steady state (in percent). Turquoise lines show the model  
1353 results using configuration OCN-LND (without sediments) and brown lines are configuration ALL (with sediments).  
1354 The y-axis on the left-hand side of each panel refers to changes in the  $^{14}\text{C}$  inventory, whereas the y-axis on the right-  
1355 hand side of each panel refers to changes in the carbon inventory or flux.

1356  
1357  
1358  
1359  
1360  
1361  
1362  
1363  
1364  
1365  
1366  
1367  
1368  
1369  
1370  
1371  
1372  
1373  
1374  
1375  
1376  
1377  
1378  
1379  
1380



1381  
 1382 Fig. 6. Change in  $\Delta^{14}\text{C}$  for the atmosphere, surface ocean, deep ocean, and global ocean for the scenarios “reduced  
 1383 deep ocean ventilation” (left) and “enhanced permanent sea ice cover” (right). Anomalies are expressed here as  
 1384 differences relative to the preindustrial steady state (in permil). Turquoise lines show the model results using  
 1385 configuration OCN-LND (without sediments) and brown lines are configuration ALL (with sediments).

1386



1387  
 1388 Fig. 7. Component of atmospheric  $\Delta^{14}\text{C}$  variability caused by production changes alone. (a) Relative  $^{14}\text{C}$  production  
 1389 rate as inferred from paleointensity data (gray) and from polar ice-core  $^{10}\text{Be}$  fluxes (purple). The heavy dark gray line  
 1390 is the mean paleointensity-based  $^{14}\text{C}$  production rate. (b) Modelled  $\Delta^{14}\text{C}$  records based only on  $^{14}\text{C}$  production changes,  
 1391 compared with the reconstructed IntCal13 and Hulu Cave  $\Delta^{14}\text{C}$  records. The modelled records are given by scenario  
 1392 MOD that assumes a constant preindustrial carbon cycle. (c) Difference between reconstructed  $\Delta^{14}\text{C}$  and model-  
 1393 simulated  $\Delta^{14}\text{C}$  using averaged paleointensity data (RPI-based  $\Delta\Delta^{14}\text{C}$ ; gray) and the ice-core  $^{10}\text{Be}$  data of Adolphi et

1394 al. (2018) ( $^{10}\text{Be}$ -based  $\Delta\Delta^{14}\text{C}$ ; purple), compared with the atmospheric  $\text{CO}_2$  record (red). Solid lines show the  
1395 IntCal13–model difference, whereas dashed lines show the Hulu–model difference. The  $\Delta\Delta^{14}\text{C}$  curve indicates  
1396 changes in  $\Delta^{14}\text{C}$  that can be attributed to some combination of carbon cycle changes, uncertainties in the reconstruction  
1397 of the  $^{14}\text{C}$  production rate, and uncertainties in the IntCal13 and Hulu Cave  $\Delta^{14}\text{C}$  records.

1398

1399

1400

1401

1402

1403

1404

1405

1406

1407

1408

1409

1410

1411

1412

1413

1414

1415

1416

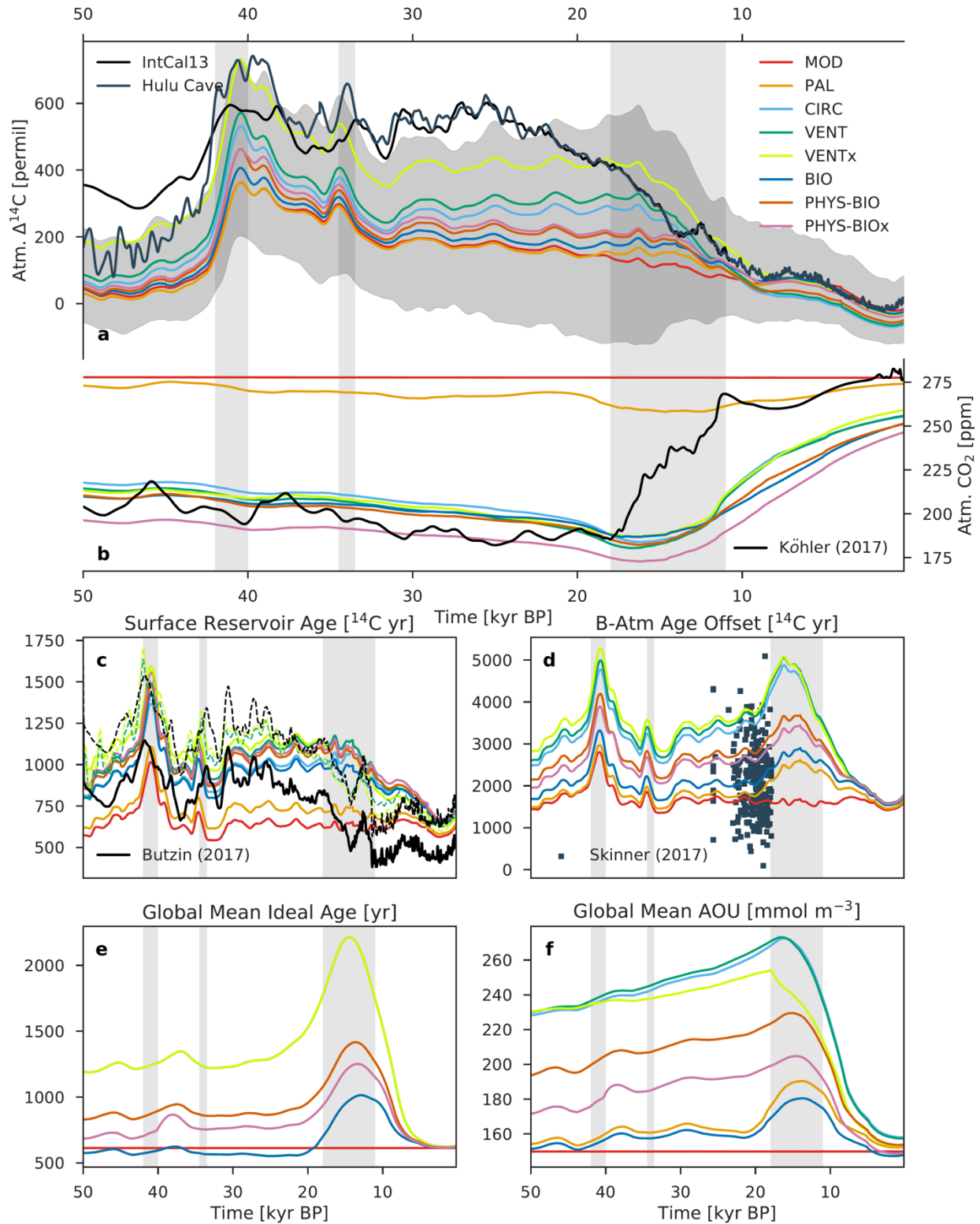
1417

1418

1419

1420

1421



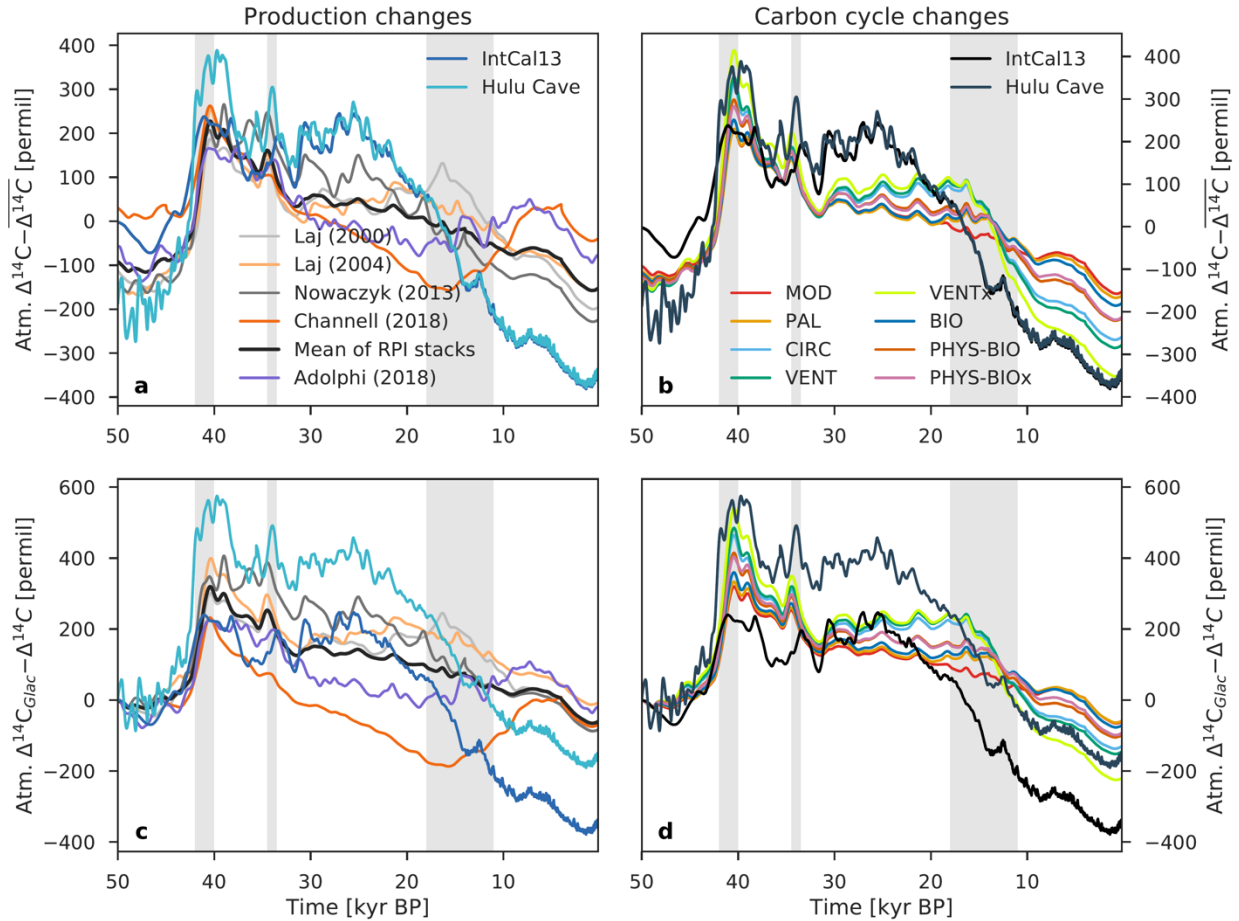
1422  
 1423  
 1424  
 1425

Fig. 8. Modelled records of atmospheric (a)  $\Delta^{14}\text{C}$  and (b)  $\text{CO}_2$ , compared with their reconstructed histories (black and dark blue lines). Also shown are modelled records of the global average (c) surface reservoir age and (d) B-Atm  $^{14}\text{C}$  age offset, compared with a recent compilation of LGM marine radiocarbon data (dark blue squares) by Skinner et al.

1426 (2017) and model-based surface reservoir age estimates between 50°N and 50°S (solid black line) and across all  
1427 latitudes (dashed black line) from Butzin et al. (2017), as well as (e) ideal age and (f) apparent oxygen utilization  
1428 (AOU). Colored lines show the results of model runs using the mean paleointensity-based  $^{14}\text{C}$  production rate and the  
1429 eight different carbon cycle scenarios described in Sect. 2.4 and Table 1. The gray envelope in (a) shows the  
1430 uncertainty ( $2\sigma$ ) from all production rate reconstructions and carbon cycle scenarios, providing a bounded estimate of  
1431  $\Delta^{14}\text{C}$  change. The dashed colored lines in (c) show the surface reservoir age results from VENT and VENTx where  
1432 atmospheric  $\Delta^{14}\text{C}$  and  $\text{CO}_2$  are prescribed. Radiocarbon ventilation ages are expressed here as radiocarbon reservoir  
1433 age offsets following Soulet et al. (2016) which are used extensively by the radiocarbon dating community.

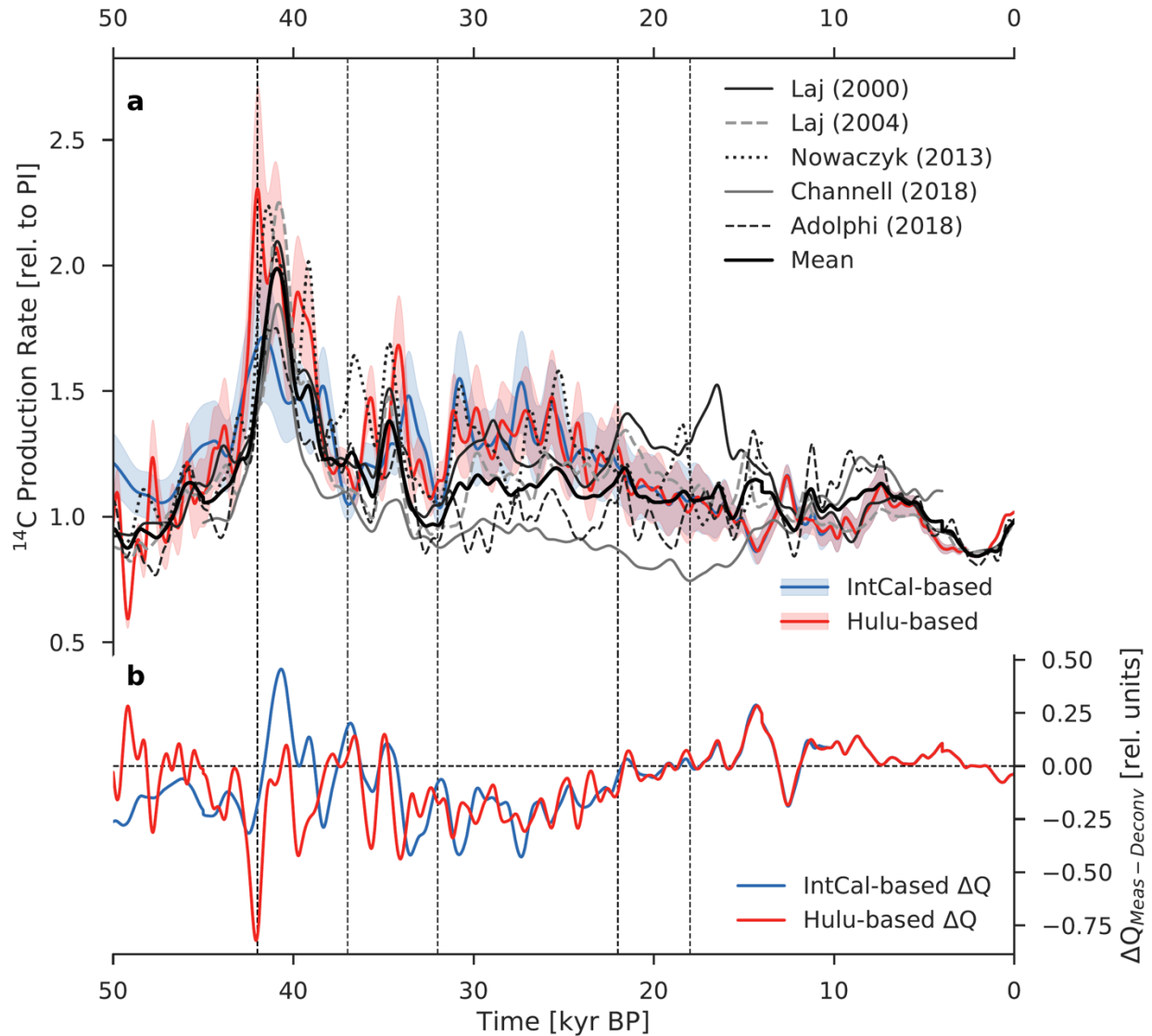
1434  
1435  
1436  
1437  
1438  
1439  
1440  
1441  
1442  
1443  
1444  
1445  
1446  
1447  
1448  
1449  
1450  
1451  
1452  
1453  
1454  
1455  
1456  
1457  
1458  
1459





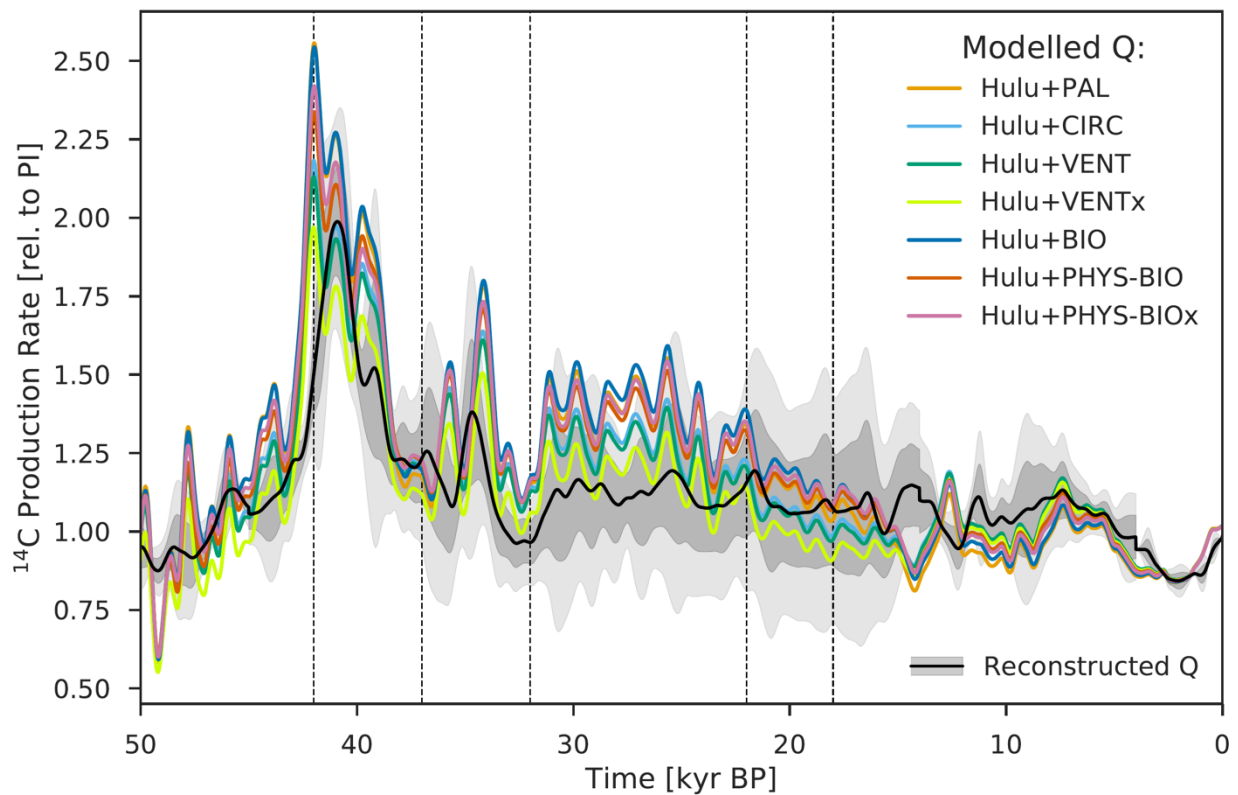
1460  
 1461 Fig. 9. Comparison of atmospheric  $\Delta^{14}\text{C}$  variability caused by changes in the ocean carbon cycle (b, d) with  
 1462 production-driven changes in atmospheric  $\Delta^{14}\text{C}$  using scenario MOD (a, c). For the analysis of carbon cycle changes,  
 1463 only the results of model runs using the mean paleointensity-based  $^{14}\text{C}$  production rate are shown. The  $\Delta^{14}\text{C}$  records  
 1464 in the upper panel (a, b) have been detrended by removing the mean, whereas the lower panel (c, d) shows  $\Delta^{14}\text{C}$   
 1465 anomalies expressed as differences relative to the  $\Delta^{14}\text{C}$  value at 50 kyr BP. Three vertical light gray bars indicate the  
 1466 Laschamp ( $\sim 41$  kyr BP) and Mono Lake ( $\sim 34$  kyr BP) geomagnetic excursions, and the last glacial termination ( $\sim 18$   
 1467 to 11 kyr BP).

1468  
 1469  
 1470  
 1471  
 1472  
 1473



1474  
 1475 Fig. 10. Comparison of  $^{14}\text{C}$  production rate estimates inferred from a deconvolution of the atmospheric  $\Delta^{14}\text{C}$  record  
 1476 and from paleointensity and ice-core  $^{10}\text{Be}$  data. (a)  $^{14}\text{C}$  production rate calculated as the sum of the modelled air-sea  
 1477 and atmosphere-land  $^{14}\text{CO}_2$  fluxes and the reconstructed change in the atmospheric  $^{14}\text{C}$  inventory and loss of  $^{14}\text{C}$  due  
 1478 to radioactive decay (see Eq. [2]). Model-based  $^{14}\text{CO}_2$  fluxes were obtained by forcing the Bern3D carbon cycle model  
 1479 with reconstructed variations in atmospheric  $\Delta^{14}\text{C}$  and  $\text{CO}_2$  as well as seven different carbon cycle scenarios. Results  
 1480 of model runs using the IntCal13 calibration curve are shown in the light blue envelope ( $2\sigma$ ), whereas the light red  
 1481 envelope ( $2\sigma$ ) shows the results from simulations using the composite Hulu Cave (10.6 to 50 kyr BP) and IntCal13 (0  
 1482 to 10.6 kyr BP)  $\Delta^{14}\text{C}$  record. The heavy black line is the mean of five available production rate reconstructions: Laj et  
 1483 al. (2000), Laj et al. (2004), Nowaczyk et al. (2013), Channell et al. (2018), and Adolphi et al. (2018). (b) Difference  
 1484 between the mean of the measurement-based production rate estimates (heavy black line) and estimates based on the  
 1485 deconvolution of the IntCal13 (IntCal-based  $\Delta Q$ ; blue) and Hulu Cave (Hulu-based  $\Delta Q$ ; red)  $\Delta^{14}\text{C}$  data.

1486



1487  
 1488 Fig. 11. Relative  $^{14}\text{C}$  production rate as inferred from the Bern3D model under seven carbon cycle scenarios (see Sect.  
 1489 2.4). Estimates shown here are based on the composite Hulu Cave and IntCal13  $\Delta^{14}\text{C}$  record. The black line is the  
 1490 mean of the five production rate reconstructions shown in Fig. 10; the gray envelope shows its uncertainty ( $2\sigma$ ).

1491  
 1492  
 1493  
 1494  
 1495  
 1496  
 1497  
 1498  
 1499  
 1500  
 1501  
 1502  
 1503  
 1504  
 1505